



SENSORCOMM 2020

The Fourteenth International Conference on Sensor Technologies and
Applications

ISBN: 978-1-61208-819-8

November 21 - 25, 2020

SENSORCOMM 2020 Editors

Anne-Lena Kampen, Western Norway University of Applied Sciences, Norway
Cosmin Dini, IARIA, EU/USA

Pedro V. Mauri, Instituto Madrileño de Investigación y Desarrollo Rural, Agrario y
Alimentario (IMIDRA), Spain

SENSORCOMM 2020

Forward

The Fourteenth International Conference on Sensor Technologies and Applications (SENSORCOMM 2020), held on November 21-25, 2020, was a multi-track event covering related topics on theory and practice on wired and wireless sensors and sensor networks.

Sensors and sensor networks have become a highly active research area because of their potential of providing diverse services to broad range of applications, not only on science and engineering, but equally importantly on issues related to critical infrastructure protection and security, health care, the environment, energy, food safety, and the potential impact on the quality of all areas of life.

Sensor networks and sensor-based systems support many applications today on the ground. Underwater operations and applications are quite limited by comparison. Most applications refer to remotely controlled submersibles and wide-area data collection systems at a coarse granularity.

In wireless sensor and micro-sensor networks energy consumption is a key factor for the sensor lifetime and accuracy of information. Protocols and mechanisms have been proposed for energy optimization considering various communication factors and types of applications. Conserving energy and optimizing energy consumption are challenges in wireless sensor networks, requiring energy-adaptive protocols, self-organization, and balanced forwarding mechanisms.

We take here the opportunity to warmly thank all the members of the SENSORCOMM 2020 technical program committee, as well as all the reviewers. The creation of such a high quality conference program would not have been possible without their involvement. We also kindly thank all the authors who dedicated much of their time and effort to contribute to SENSORCOMM 2020. We truly believe that, thanks to all these efforts, the final conference program consisted of top quality contributions.

We also thank the members of the SENSORCOMM 2020 organizing committee for their help in handling the logistics and for their work that made this professional meeting a success.

We hope that SENSORCOMM 2020 was a successful international forum for the exchange of ideas and results between academia and industry and to promote further progress in the area of sensor technologies and applications.

SENSORCOMM 2020 Chairs

SENSORCOMM 2020 General Chair

Jaime Lloret Mauri, Polytechnic University of Valencia, Spain

SENSORCOMM 2020 Publicity Chair

Lorena Parra, Universitat Politecnica de Valencia, Spain // Instituto Madrileño de Investigación y Desarrollo Rural, Agrario y Alimentario (IMIDRA), Madrid, Spain

Jose Luis García, Universitat Politecnica de Valencia, Spain

SENSORCOMM 2020

Committee

SENSORCOMM 2020 General Chair

Jaime Lloret Mauri, Polytechnic University of Valencia, Spain

SENSORCOMM 2020 Publicity Chair

Lorena Parra, Universitat Politècnica de Valencia, Spain // Instituto Madrileño de Investigación y Desarrollo Rural, Agrario y Alimentario (IMIDRA), Madrid, Spain
Jose Luis García, Universitat Politècnica de Valencia, Spain

SENSORCOMM 2020 Technical Program Committee

Majid Bayani Abbasy, National University of Costa Rica, Costa Rica
Amin Al-Habaibeh, Nottingham Trent University, UK
Jesús B. Alonso Hernández, Institute for Technological Development and Innovation in Communications (IDeTIC) | University of Las Palmas de Gran Canaria (ULPGC), Spain
Mário Alves, Politécnico do Porto - School of Engineering (ISEP), Portugal
Thierry Antoine-Santoni, University of Corsica, France
Kazutami Arimoto, Okayama Prefectural University, Japan
Anish Arora, The Ohio State University / The Samraksh Company, USA
Andy Augousti, Kingston University London, UK
Michel Bakni, ESTIA Recherche, Bidart, France
Reda Benkhouya, Ibn Tofail University, Morocco
Souheila Bouam, University of Batna 2, Algeria
An Braeken, Vrije Universiteit België, Belgium
Erik Buchmann, Hochschule für Telekommunikation Leipzig, Germany
Juan-Vicente Capella-Hernández, Universitat Politècnica de València, Spain
Vítor Carvalho, 2Ai Lab- School of Technology - IPCA / Algoritmi Research Center - Minho University, Portugal
Mario Cifrek, University of Zagreb, Croatia
Federico Corò, Sapienza University of Rome, Italy
Luis J. de la Cruz Llopis, Universitat Politècnica de Catalunya, Spain
Baban P. Dhonge, Indira Gandhi Center for Atomic Research, Kalpakkam, India
Alexis Duque, Rtone, Lyon, France
Loubna El Amrani, Ibn University Tofail Kénitra, Morocco
Mohamed El Bakkali, Sidi Mohamed Ben Abdellah University, Morocco
Youssef Elgholb, University Sidi Mohamed Ben Abdellah, Fez, Morocco / Technical University of Cartagena, Spain
Biyi Fang, Microsoft Corporation, USA
Stefan Fischer, University of Lübeck, Germany
Fernando Juan García-Diego, Universitat Politècnica de València, Spain
Dinesh R. Gawade, Tyndall National Institute | University College Cork, Ireland

Xiaocheng Ge, University of Huddersfield, UK
Lyamine Guezouli, University of Batna 2, Algeria
Arda Gumusalan, IBM, USA
Malka N. Halgamuge, The University of Melbourne, Australia
Chitra Javali, Institute for Infocomm Research (I2R) - A*STAR, Singapore
Miao Jin, University of Louisiana at Lafayette, USA
Anand Y Joshi, G. H. Patel College of Engineering and Technology, India
Grigoris Kaltsas, University of West Attica, Greece
Lutful Karim, Seneca College of Applied Arts and Technology, Toronto, Canada
Azeddine Khiat, ENSET Mohammedia | University Hassan II of Casablanca, Morocco
Boris Kovalerchuk, Central Washington University, USA
Prasan Kumar Sahoo, Chang Gung University, Taiwan
Chiu-Kuo Liang, Chung Hua University, Hsinchu, Taiwan
David Lizcano, Madrid Open University (UDIMA), Spain
Flaminia Luccio, University Ca' Foscari of Venice, Italy
Abdalah Makhoul, University of Franche-Comté, France
Piero Malcovati, University of Pavia, Italy
Stefano Mariani, Politecnico di Milano, Italy
Jose-Manuel Martinez-Caro, Technical University of Cartagena, Spain
Carlo Massaroni, Università Campus Bio-Medico di Roma, Italy
Lei Mei, KLA Corporation, USA
Carosena Meola, University of Naples Federico II, Italy
Fabien Mieyeville, Polytech Lyon - University Claude Bernard Lyon 1, France
Raúl Monroy, Tecnológico de Monterrey, Mexico
Rafael Morales Herrera, Universidad de Castilla-La Mancha, Spain
Dmitry Namiot, Lomonosov Moscow State University, Russia
Jagriti Narang, Jamia Hamdard, New Delhi, India
Mir Mohammad Navidi, West Virginia University, USA
Michael Niedermayer, Beuth University of Applied Sciences, Germany
Rosdiadee Nordin, Universiti Kebangsaan Malaysia, Malaysia
Brendan O'Flynn, Tyndall National Institute | University College Cork, Ireland
Pouya Ostovari, San Jose State University | Charles W. Davidson College of Engineering, USA
Carlos Enrique Palau Salvador, Universitat Politècnica de València, Spain
Carlos Penichet, Uppsala University, Sweden
Ivan Miguel Pires, Instituto de Telecomunicações - Universidade da Beira Interior / Polytechnic Institute of Viseu, Portugal
Patrick Pons, LAAS-CNRS, France
Càndid Reig, University of Valencia, Spain
Girish Revadigar, Huawei International Pte Ltd, Singapore
Christos Riziotis, National Hellenic Research Foundation, Greece
Lorenzo Rubio Arjona, Universitat Politècnica de València, Spain
Ulrich Rückert, Bielefeld University, Germany
Sain Saginbekov, Nazarbayev University, Nur-Sultan, Kazakhstan
Addisson Salazar, Universitat Politècnica de València, Spain
Sheng Shen, University of Illinois at Urbana-Champaign, USA
Francesco Betti Sorbelli, Missouri University of Science & Technology, USA
Mu-Chun Su, National Central University, Taiwan
Alvaro Suárez Sarmiento, University of Las Palmas de Gran Canaria, Spain

Rui Teng, Advanced Telecommunications Research Institute International, Japan
Carlos Travieso González, University of Las Palmas de Gran Canaria, Spain
Yu Chee Tseng, NCTU, Taiwan
Manuela Vieira, CTS/ISEL/IPL, Portugal
You-Chiun Wang, National Sun Yat-sen University, Taiwan
Julian Webber, Osaka University, Japan
Murat Kaya Yapici, Sabanci University, Turkey
Sergey Y. Yurish, International Frequency Sensor Association (IFSA), Spain
Zhe Zhou, Huzhou University, China
Chengzhi Zong, eBay Inc, USA

Copyright Information

For your reference, this is the text governing the copyright release for material published by IARIA.

The copyright release is a transfer of publication rights, which allows IARIA and its partners to drive the dissemination of the published material. This allows IARIA to give articles increased visibility via distribution, inclusion in libraries, and arrangements for submission to indexes.

I, the undersigned, declare that the article is original, and that I represent the authors of this article in the copyright release matters. If this work has been done as work-for-hire, I have obtained all necessary clearances to execute a copyright release. I hereby irrevocably transfer exclusive copyright for this material to IARIA. I give IARIA permission to reproduce the work in any media format such as, but not limited to, print, digital, or electronic. I give IARIA permission to distribute the materials without restriction to any institutions or individuals. I give IARIA permission to submit the work for inclusion in article repositories as IARIA sees fit.

I, the undersigned, declare that to the best of my knowledge, the article does not contain libelous or otherwise unlawful contents or invading the right of privacy or infringing on a proprietary right.

Following the copyright release, any circulated version of the article must bear the copyright notice and any header and footer information that IARIA applies to the published article.

IARIA grants royalty-free permission to the authors to disseminate the work, under the above provisions, for any academic, commercial, or industrial use. IARIA grants royalty-free permission to any individuals or institutions to make the article available electronically, online, or in print.

IARIA acknowledges that rights to any algorithm, process, procedure, apparatus, or articles of manufacture remain with the authors and their employers.

I, the undersigned, understand that IARIA will not be liable, in contract, tort (including, without limitation, negligence), pre-contract or other representations (other than fraudulent misrepresentations) or otherwise in connection with the publication of my work.

Exception to the above is made for work-for-hire performed while employed by the government. In that case, copyright to the material remains with the said government. The rightful owners (authors and government entity) grant unlimited and unrestricted permission to IARIA, IARIA's contractors, and IARIA's partners to further distribute the work.

Table of Contents

Energy Harvesting Wireless Sensor Network Edge Device Simulation Tool <i>Cian O'Shea, Ross O'Halloran, Peter Haigh, and Mike Hayes</i>	1
Reducing The Energy Consumed During Multihop Transmissions in Wireless Sensor Networks <i>Anne-Lena Kampen and Knut Ovsthus</i>	11
Inductive Communication and Localization Method for Wireless Sensors in Photobioreactors <i>David Demetz and Alexander Sutor</i>	19
Towards Joint Cell Selection and Task Offloading in Cellular IoT Systems with Edge Computing <i>Edgar Adrian Esquivel-Mendiola, Sergio Perez-Picazo, and Hiram Galeana-Zapien</i>	23
Rapid Detection of Toxic Emissions Using DNN Based Sensing <i>Ibrahim Bhavnagarwala and Adam Bhavnagarwala</i>	28
IMPAQT Miniaturized Underwater Acoustic Telemetry Platform: Transmitter Node System Design <i>Hamed Jafarzadeh, Marco Belcastro, and Brendan O'Flynn</i>	34

Energy Harvesting Wireless Sensor Network Edge Device Simulation Tool

Cian O'Shea, Ross O'Halloran, Peter Haigh, Mike Hayes
 Tyndall National Institute
 Cork, Ireland
 Email: cian.oshea@tyndall.ie

Abstract - Wireless Sensor Networks (WSN) are becoming widely adopted in many industries including health care, building energy management and conditional monitoring. As the scale of low-power sensor network deployments increases, the cost and complexity of battery replacement and disposal have become more significant and in time may become a barrier to adoption. Harvesting ambient energies provides a pathway to reducing dependence on batteries and for many application scenarios, may lead to autonomously powered sensors. This work describes a simulation tool that enables the user to predict the battery life of a wireless sensor that utilizes energy harvesting to supplement the battery power. To create this simulator, all aspects of a typical WSN edge device (node) were modelled including sensors, transceiver and microcontroller as well as the energy source components (batteries, solar (PV) cells, Thermoelectric Generators (TEG), supercapacitors and DC/DC converters). The tool allows the user to plug and play different pre-characterized devices as well as add user defined devices. The goal of this simulation tool is to provide a WSN installer with a methodology to deploy systems with optimum battery lifetime by scaling battery and energy harvesting component sizes appropriately for a given scenario. It also allows a component designer to examine trade-offs in system level performance versus device specifications for optimum battery lifetime.

Keywords – *Wireless Sensor Network; Low-power sensor network; Internet of Things (IoT); Energy Harvester; simulation tool*

I. INTRODUCTION

With the ever-increasing push to have a more energy efficient environment, the retrofit of IoT edge devices, such as wireless sensors in, on or near equipment and its operating environment is becoming more prevalent to help gather data to achieve this goal. Commercial and residential buildings are now expected to meet better and higher standards of energy efficiency, with the Irish government mandating that all newly constructed buildings require at least 20% of the energy needs be sourced through renewable energy [1].

The deployment of IoT devices is growing at an exponential rate. By 2025 there will be an estimated 75 billion IoT devices worldwide [2] most of which, will be wireless. One of the biggest challenges that IoT devices face is battery life. With so many devices globally, this is a serious issue. According to the United States Environmental Protection Agency, roughly 90% of batteries are recycled [3]. By 2025, that still leaves 7.5 billion batteries filling landfills and polluting the earth.

Combine this with the environmental cost of mining the material used and the monetary cost of producing so many batteries, technologies such as energy harvesting that enable battery life to be extended are highly desirable. The simulation tool presented in this paper will allow a user to select from a range of different components to extend the battery life of their IoT end nodes by installing more cost effective, lower maintenance overhead and energy efficient device.

Energy harvesting is the act of collecting ambient energy from the environment and either converting it into device-ready electrical energy or storing it. The environment has readily available ambient sources of energy. Energy harvesting can be very beneficial for WSN nodes. This software tool will allow people to see the usefulness of energy harvesting and how real-world applications can be completely powered or have their battery life extended with the use of an energy harvesting system. This tool will encourage the use of ambient energies, particularly in applications that would greatly benefit from averting or prolonging the need for battery replacement, for example in hard to reach areas such as civil engineering structures and medical implants.

In Section 2 this paper will present the simulation tool and discuss its operation. Section 3 will then describe WSN and the different components involved. Section 4 will present the user interface of the simulation tool and illustrate what a typical user would see. Sections 5 to 10 will then describe each component and its characterization methods. The results in Section 11 will show a comparison between a real-world test and software simulation, showing the accuracy of the tool. The final Section will present the conclusions drawn and propose several possible directions for future work.

II. SOFTWARE TOOL

Energy harvesting is a common method used to extend the battery lifetime in WSN devices. The software application described in this paper has two purposes:

1. It can be used by component designers to trade off system performance against component performance in an end node.
2. It can also be used by a system integrator as a validation tool during the development process of the WSN system. It will allow a user to determine if the ambient energy available to the

device is enough to sustain it or prolong the battery lifetime for a desired period.

One of the main goals of this software tool was to have the ability to predict lifetime for any given node. This allows a user to import any type of component to the software using the predetermined characterisation structure and predict the lifetime of the WSN node using a given combination of power generation, storage and consumption components.

III. WIRELESS SENSOR NETWORK

A WSN consists of a gateway, which receives all of the data from the connected nodes in the network and then transmits that data to the cloud, as shown in Figure 1.

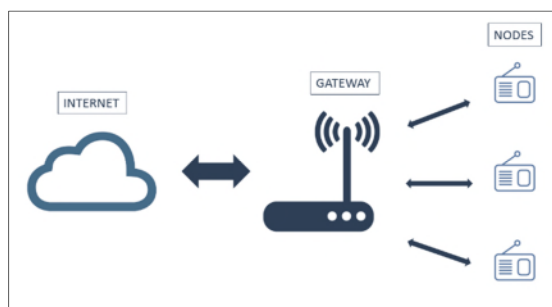


Figure 1. Example of a WSN.

The focus of this simulation tool is predicting the lifetime of the nodes in the network by importing characterized components and flowing that data through a set of equations to accurately predict the lifetime of the device. A typical node in a WSN that utilizes Energy Harvesting (EH-WSN) methods consists of the following parts; an energy harvester, a power-management IC, which includes a Maximum Power Point Tracker (MPPT), an energy storage device, a DC-DC converter and finally a sensor (or cluster of sensors).

Figure 2 represents a block diagram of an EH-WSN.

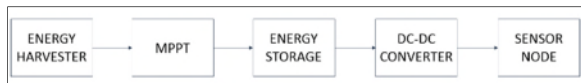


Figure 2. EH-WSN block diagram.

The energy harvester transducers that are available with the simulation tool developed are PV cells and TEGs. With the ambient energy available (e.g., light, heat) usually being quite limited and sporadic, any change in environmental conditions throughout the harvesting period can have a significant effect on the amount of energy that the EH (energy harvesting) transducers can provide. For this reason, an MPPT circuit is required to maximise the power output from the transducer to the load. Because of the uncertainty in available power from

energy harvesting, an energy storage device is required to maintain constant power to the sensor node. An energy storage device can provide power to the load when the ambient energy is unavailable, but it can also, store excess energy when the transducers are harvesting more energy than the load requires. Supercapacitors, also known as ultracapacitors or double-layer capacitors, are commonly used in EH-WSNs as they have a higher power density than batteries and can operate without the need for additional charging circuitry. They also have a long operational lifetime, with charging and discharging of the device having little to no effect on it [4]. However, as the voltage in the device is varying, a DC-DC converter is required to maintain a stable voltage on the sensor node, which typically contains a receiver, transmitter and a microprocessor. Primary batteries are also used for energy storage, with the choice being dependent on application powering requirements. These additional batteries may also require a DC-DC converter.

IV. GUI

When the application launches, the user can vary any of the parameters in a WSN by selecting the button that corresponds to that section. These buttons can be seen in Figure 3.

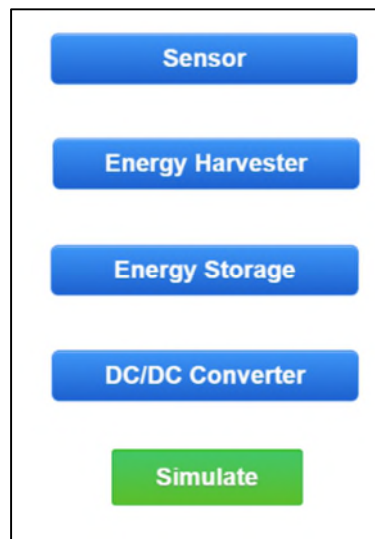


Figure 3. GUI buttons.

In Figure 4, the user can input the operating voltage and the average current consumption of the device which then gets sent to the main simulation file and awaits further data.

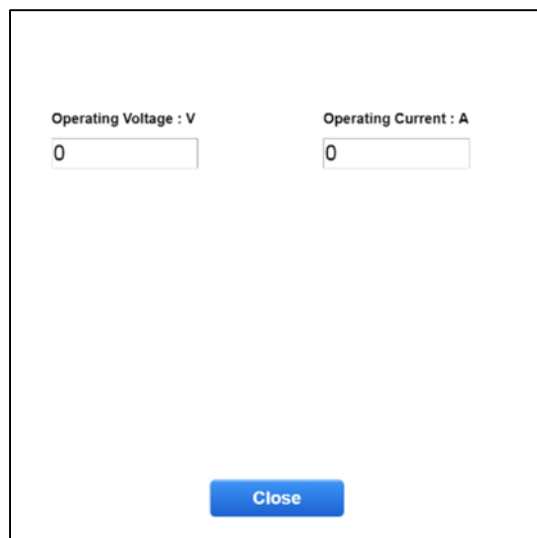


Figure 4. Sensor Node menu.

The two types of EH devices available in this simulation tool are PV cells and TEGs whose parameters can be modified in Figure 5. Other types can be easily added. The user can select which type and then either select from pre-characterised components in the tool or add a new component to the simulation. This allows users to import their own components to test their viability in a WSN system. The size of the components and ambient conditions must also be selected.

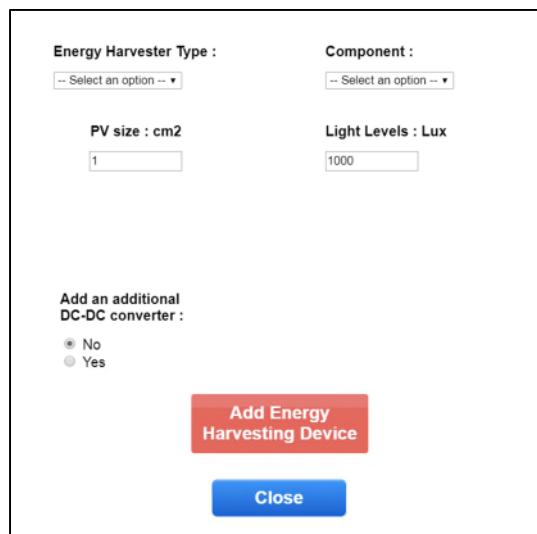


Figure 5. EH menu.

Similar to the EH section, Figure 6 shows that the user can enter the parameters of the supercapacitor or import a new component. The minimum and turn on voltage of the supercapacitor can also be selected. This notifies the simulation that once the supercapacitor reaches the minimum voltage, it must be allowed time to recharge

back to the turn on voltage and disconnected from the load. This allows the system to alternate between powering the sensor node using EH methods and using battery power.

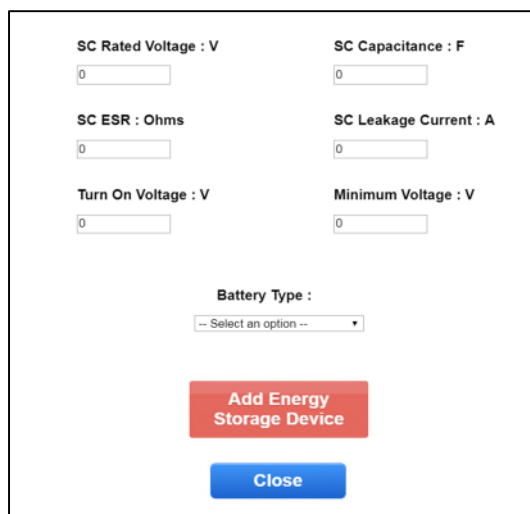


Figure 6. Supercapacitor menu.

Figure 7 shows a selection window for a DC-DC converter. As was mentioned previously, the system requires a DC-DC converter to maintain a constant voltage to the sensor node. Depending on the minimum and maximum input voltages of the device, it may influence the operating limits of the supercapacitor. The rated voltage of the supercapacitor should be checked to see if it is compatible with the DC-DC converter.



Figure 7. DC-DC converter menu.

Once all of the parameters are selected, a simulation window is presented to the user. Figure 8 shows a complete simulation, illustrating the effects of the

minimum and turn-on voltages. Figure 9 compares the lifetime of the device when powered solely by battery (shown in red) and a battery-EH hybrid system (shown in blue).

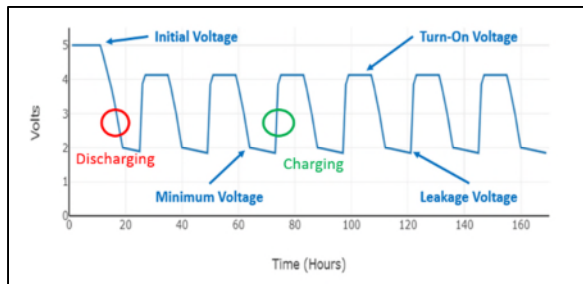


Figure 8. Supercapacitor voltage over time.

As the simulation is running, the graph presented in Figure 8 is shown. This allows the user to see when the supercapacitor reaches its minimum or maximum voltage and can alter the components to achieve the optimum power solution to the device, whether the supercapacitor is receiving too much energy or too little. It also allows the user to check whether or not the supercapacitor is sized correctly or the DC-DC converter suitable for the system. Figure 8 also shows that when the supercapacitor reaches the minimum voltage and there is no ambient energy available, the voltage continues to drop due to leakage current before the charging cycle starts again.

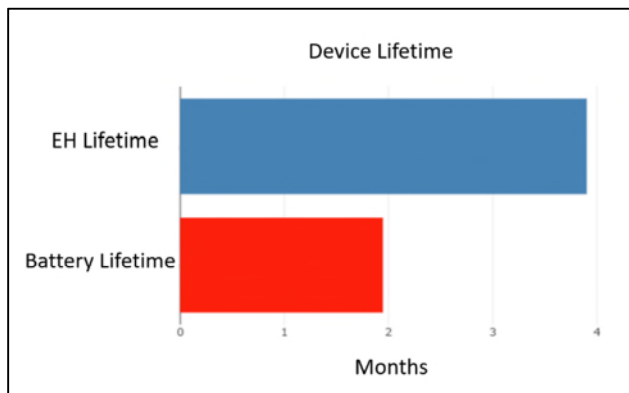


Figure 9. Battery WSN vs. EH-WSN.

Altering the input parameters to the system allows the user to determine the optimised component setup to power the device.

Once the simulation has begun, bars shown in Figures 10-12 will present the ongoing conditions in the system over time. When there is no ambient energy available to the system (e.g., lights switched off), the yellow bar is depleted signalling that the supercapacitor is no longer receiving energy. This can be seen as the simulation is

displayed. Figure 11 is a representation of the green circle shown in Figure 8. The device is receiving ambient energy and charging. Figure 12 is a representation of the red circle. There is no ambient energy available and the supercapacitor is roughly 50% charged.

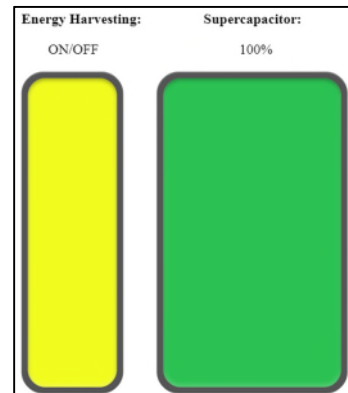


Figure 10. Simulation dynamic conditions.

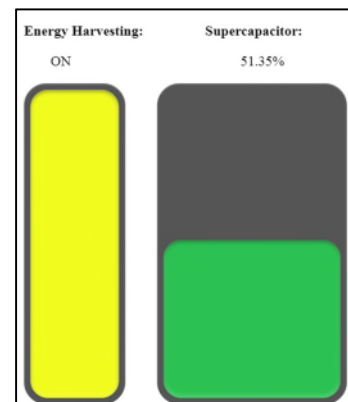


Figure 11. Simulation dynamic conditions.

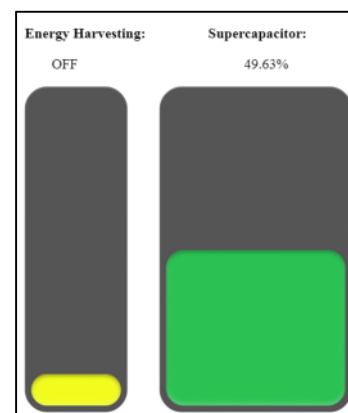


Figure 12. Simulation dynamic conditions.

As the WSN switches between the use of EH and the use of a battery, that too is shown to the user with the EH bar toggling on or off and the supercapacitor bar increasing or

decreasing. If the supercapacitor reaches the minimum voltage, it requires time to recharge, which switches the device to receive power from the battery. Figures 13 and 14 represent when the device is receiving ambient energy or not respectively.

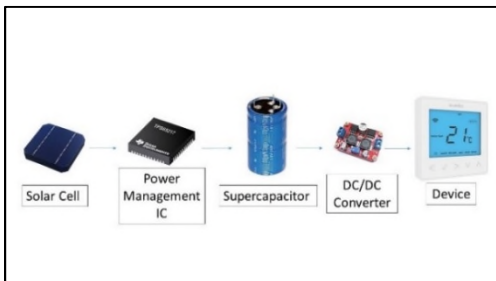


Figure 13. Using EH indicator.

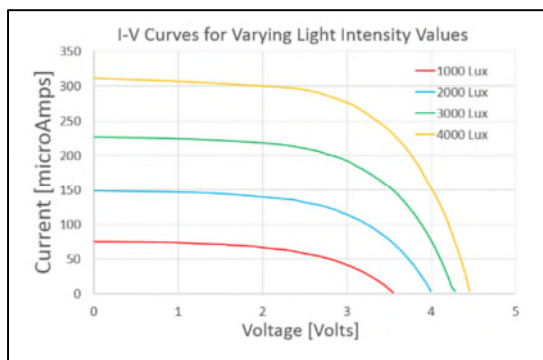


Figure 14. Using battery indicator.

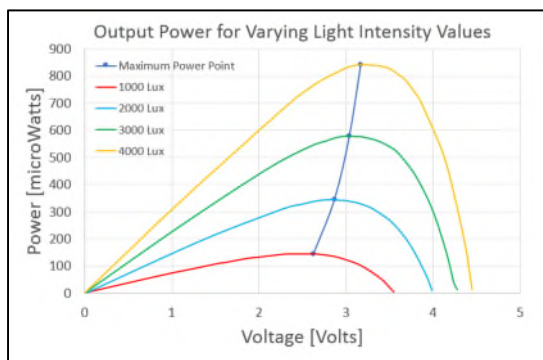
What makes this different from other WSN simulators, is its ability to import new components and allow users to use their own or test components they are thinking of acquiring. The characterisation templates are included with the software and that data can mostly be found in the datasheets of the components or easily derived from some bench testing.

V. ENERGY HARVESTER

PV cells can be characterised by using what is termed “I-V & P-V curves”. They represent the relationship between the electric current/power through the cell with the corresponding voltage for different light intensity levels. These curves can then be used to find the maximum power point.



(a)



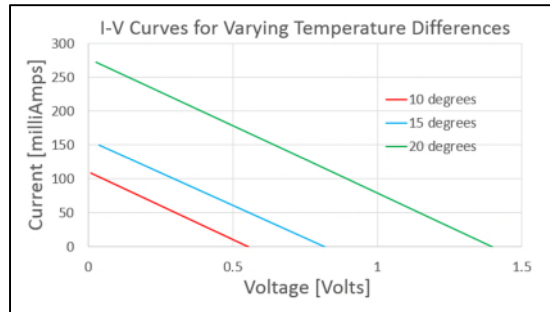
(b)

Figure 15. (a) I-V curves for varying light intensity levels. (b) Output power for varying light intensity levels.

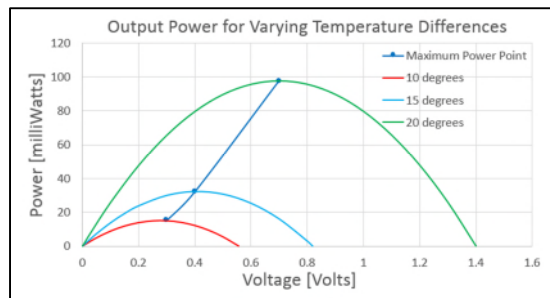
Figure 15(a) shows how different lux levels can affect the current generated by the PV cell whilst Figure 15(b) presents the maximum output power of the PV cell for each lux value. An MPPT circuit can be used to help the PV cell operate at its maximum power point.

Thermoelectric generators work by taking advantage of the Seebeck effect, which directly converts temperature difference into electricity. When heat is applied to one of the two conductors in the TEG, the temperature of electrons close to the surface begin to rise and flow towards the cooler surface creating current flow. When a temperature difference exists on the P-N junctions, a potential voltage difference between the hot and cold surfaces occurs [5].

Similarly to a PV cell, a TEG is also characterised using “I-V curves” and “P-V curves” and impedance matching circuits can be used to obtain a maximum power point, which can be seen in Figures 16 (a) & (b).



(a)



(b)

Figure 16. (a) I-V curves for varying temperature differences. (b) Output power for varying temperature differences.

VI. MAXIMUM POWER POINT TRACKER FOR PV

The MPPT used in this simulation tool for PV is called Fractional Open-Circuit Voltage (FOCV). This method is based on the fact that the voltage of the PV cell at the maximum power point (V_{MPP}) is approximately linearly proportional to the open-circuit voltage (V_{OC}) and short-circuit current (I_{SC}) based on the following equations:

$$V_{MPP} \approx K_1 * V_{OC} \quad (1)$$

$$I_{MPP} \approx K_2 * I_{SC} \quad (2)$$

where the value for K_1 ranges from 0.7-0.9 and K_2 ranges from 0.78-0.92 depending on the overall characteristics of the solar cell.

A flowchart of the FOCV algorithm is represented in Figure 17.

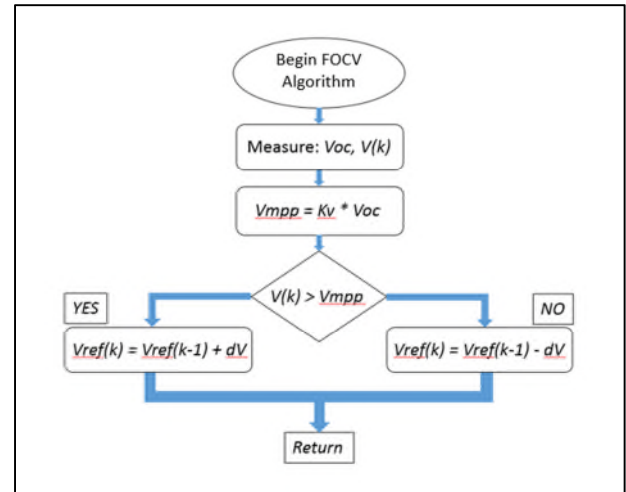


Figure 17. Fractional Open-Circuit Voltage algorithm.

From [6]-[8], it was concluded that the FOCV method was the best fit for ultra-low-power sensor networks (sub mW power levels) with an accuracy rating of 96%, which is the value used in this simulation tool.

$$MPP_{CHARACTERIZED} * 0.96 \approx P_{EH} \quad (3)$$

Where $MPP_{CHARACTERIZED}$ is maximum characterized power of the EH after it has gone through a MPPT circuit and P_{EH} is the EH power used in the simulation.

VII. ENERGY STORAGE

For optimum energy efficiency, an energy storage device is required to store any excess energy generated by the energy harvester transducers. This stored power can then be used to power the sensor node when ambient energies are no longer available in order to prolong the lifetime of the battery. A battery is used when ambient energy is not available, and the power stored in the supercapacitor is depleted. In this simulation tool, a supercapacitor is modelled in unison with a single-use battery. Taking values, such as capacitance, rated voltage, leakage current and Equivalent Series Resistance (ESR), the energy in the supercapacitor can be simulated as it charges and discharges. ESR is a non-ideal characteristic of a supercapacitor and can cause problems when dealing with I^2R losses and transients. The bigger the load transient, the larger the voltage drop due to ESR. The equations governing the supercapacitor in this simulation are shown in the results section.

VIII. DC-DC CONVERTER

When powering systems from ambient energy the designer should ensure that as much power as possible that is generated by the transducer is delivered to the load. Techniques to reduce power losses need to be employed. In this case the supercapacitor voltage will vary during charge and discharge, therefore a DC-DC converter is

required to ensure the load is supplied with the appropriate steady voltage level at maximum efficiency. The output power to the load is based entirely on the specified output voltage of the converter and the current consumption of the sensor node. The power required at the input is dependent on the voltage at the input. As the voltage at the input varies, so too does the efficiency of the converter. This also varies the power required from the supercapacitor to maintain constant power to the output. In this software tool, the user selects an average efficiency rating of the converter and then integrates top and bottom thresholds. At these points, when the voltage reaches those levels, the efficiency changes. This can be further explained in table 1.

TABLE I. DC-DC CONVERTER EFFICIENCY FOR DIFFERENT INPUT VOLTAGES

Input Voltage Range (V)	Efficiency (%)
5 – 4.2	84.5
4.2 – 3.6	86
< 3.6	90

$$\eta \approx \frac{Voltage_{OUT} * Current_{OUT}}{Voltage_{IN} * Current_{IN}} \quad (4)$$

where Voltage_{IN} and Current_{IN} are the input voltage and current to the DC-DC converter respectively (i.e., the WSN node).

Furthermore:

$$Supercapacitor\ Power \approx \frac{Node\ Power}{\eta} \quad (5)$$

Where ‘‘Supercapacitor Power’’ is power required by the supercapacitor to maintain constant power to the node. The efficiency value is also determined by the operating supercapacitor voltage. As the voltage in the supercapacitor changes with time, the efficiency at which the DC-DC converter converts the input power of the supercapacitor to the required power levels of the sensor node changes.

IX. SENSOR NODE

The sensors in these nodes typically have different operating modes, for which their period of operation is defined by their different duty cycles. The average power then depends on the power consumed in each operation mode as well as the time employed for each mode (i.e., the ‘duty cycle’). The simulation tool handles this by taking in the average current consumption level for a

specific duty cycle and using the operating voltage to determine the power required.

$$WSN\ Power = Voltage * Average\ Current \quad (6)$$

X. SIMULATION

To ensure that simulation results are accurate, the individual components need to be characterized in a uniform manner under operating conditions that reflect real life. The wide range of component types makes this challenging. However, by doing this, an extensive array of components can be catalogued and stored in the software for comparison and to assess their viability for different applications.

The simulation tool takes in CSV files containing the required information to model each component. These CSV files have data templates, which can be filled out and logged in the software.

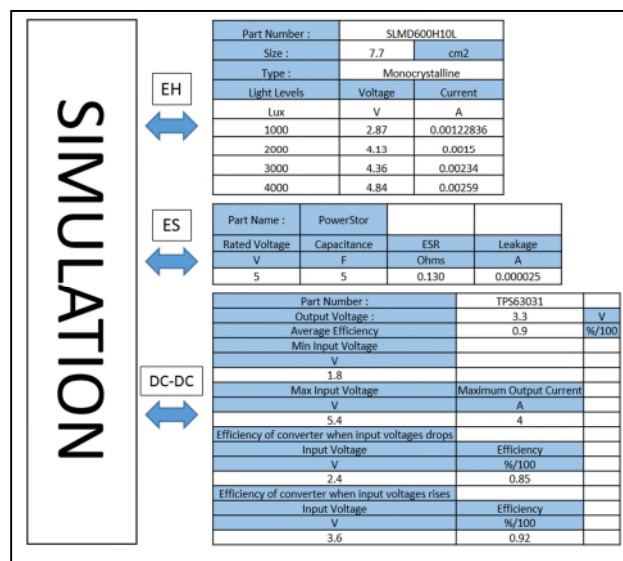


Figure 18. Component characterization templates.

Figure 18 shows the different templates for the energy harvester transducers, the energy storage devices, the DC-DC converters and the sensor nodes.

Other software tools that simulate WSNs are usually manufacturer specific. One of the unique selling features of this simulation tool is that it allows for myriads of combinations and offers the ability to add any type of component to the software.

XI. RESULTS

To test the accuracy of the simulation tool, a circuit was setup to power a LoPy4. The LoPy4 is a low-power radio module that is a typical communication device used in wireless sensors. The module supports, LoRa, Sigfox,

Bluetooth and Wi-Fi. For these experiments it was set up using LoRa.



Figure 19. LoPy4 Pycom Device.

During the test, the device shown in Figure 19 was programmed to operate at 90mA. This device was then connected to a supercapacitor, which was then connected to a power supply. Figure 20 shows the circuit schematic of the performed test with the accompanying equations. The goal of this test was to measure the voltage of the supercapacitor as it charged and discharged to compare with a simulated test under the same conditions. The voltage across the supercapacitor was recorded using a Bluno V2.0 board with a $\pm 0.15V$ error rate, connected to a laptop.

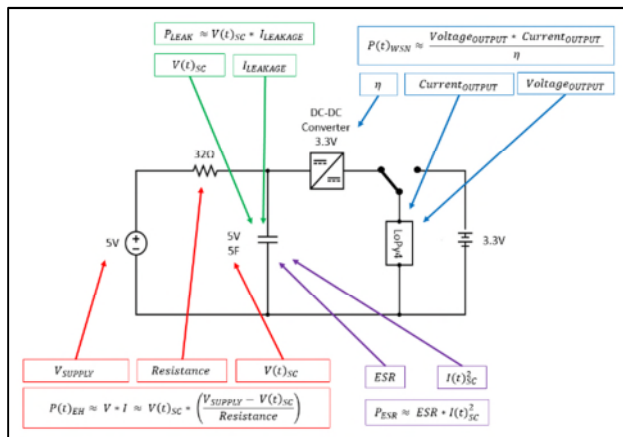


Figure 20. Circuit schematic with equation block diagram.

While the ‘pycom’ device is disconnected and receiving power from the 3V3 supply, the 32Ohm power source mimics an EH transducer. The EH power being fed to the supercapacitor can be approximated using (7). In reality, this power is feeding both the supercapacitor and the DC-DC converter that is operating in ‘no-load’ with the ‘pycom’ disconnected but this is assumed to be very small relative to the current entering the supercapacitor based in quiescent current specifications for the DC-DC converter. Power is a product of current multiplied by voltage. With the voltage constantly varying, so too was the supply current.

$$P(t)_{EH} \approx V(t)_{SC} * I(t)_R \quad (7)$$

$$P(t)_{EH} \approx V(t)_{SC} * \left(\frac{V_{SUPPLY} - V(t)_{SC}}{Resistance} \right) \quad (8)$$

Where $V(t)_{SC}$ is the voltage across the supercapacitor over time and V_{SUPPLY} is the 5V supply voltage.

When the ‘pycom’ is connected to the DC-DC converter, the current and voltage supplied at the input need to be calculated. With losses in the DC-DC converter, more power needs to be supplied than is drawn by the load. The ‘pycom’ device was set at 3.3 volts consuming 90 mA. Using the efficiency equation for DC-DC converter in (4), with the known voltage across the supercapacitor, the current supplied by the supercapacitor can be acquired.

However, as discussed previously the efficiency of the DC-DC converter is dependent on the input voltage. Using the information gathered from the datasheet, the efficiency can be calculated for different operating conditions.

The results in table 1 can then be used to calculate the power supplied to the DC-DC converter and subsequent pycom load (i.e., the WSN node) when not operating off of the 3V3 battery.

$$P(t)_{WSN} \approx \frac{Voltage_{OUTPUT} * Current_{OUTPUT}}{\eta} \quad (9)$$

$$P(t)_{WSN} \approx \frac{3.3 * 0.09}{\eta} \quad (10)$$

TABLE II. WSN NODE POWER REQUIREMENT FOR EACH DC-DC CONVERTER EFFICIENCY

Efficiency (%)	$P(t)_{WSN}$ W
84.5	0.3515
86	0.3453
90	0.33

To simplify equations, it is approximated that all of the current for the DC-DC converter comes from the supercapacitor and that the additional current coming from the 32Ohm resistor is very small. This should also offset most of the approximation error for the supercapacitor charge cycle.

The leakage current in the supercapacitor was given in the datasheet as 25 μ A and equivalent series resistance of 130m Ω . The leakage power can be calculated by multiplying leakage current by the voltage across the supercapacitor.

$$P(t)_{LEAK} \approx V(t)_{SC} * I_{LEAKAGE} \quad (11)$$

Power dissipation due to ESR in the supercapacitor can be calculated by multiplying the ESR value by the square of operating current.

$$P(t)_{ESR} \approx ESR * I(t)_{SC}^2 \quad (12)$$

All of these equations were then fed into (13).

$$E(t)_{SC} \approx E(initial)_{SC} + \int_0^t (P(t)_{EH} - P(t)_{WSN} - P(t)_{LEAK} - P(t)_{ESR}) dt \quad (13)$$

where t is the entire period for a given sensing interval. When the supercapacitor has reached its minimum energy availability, the load is disconnected, allowing the supercapacitor to recharge. The “pycom” is switched to receive power from the battery. Using the circuit presented in Figure 20, when the load is disconnected, the DC-DC converter still receives current in the form of quiescent current and the supercapacitor continues to have leakage and ESR losses. This change in current is accounted for in (14), (15) and (16).

$$P(t)_{EH} \approx V(t)_{SC} * \left(\frac{V_{SUPPLY} - V(t)_{SC}}{Resistance} - I_{DC-DC Quiescent} \right) \quad (14)$$

$$P(t)_{WSN} \approx 0 \quad (15)$$

$$P(t)_{ESR} \approx ESR * \left(\frac{V_{supply} - V(t)_{SC}}{Resistance} - I_{DC-DC Quiescent} - I_{LEAK} \right)^2 \quad (16)$$

$P(t)_{LEAK}$ during this period is still governed by (11).

From there, (17) is used to calculate the voltage in the supercapacitor and then graphed over time to allow the user to continually refine the component parameters in the software.

$$V(t)_{SC} \approx \sqrt{\frac{2 * E(t)_{SC}}{c}} \quad (17)$$

Using the minimum voltage specifications from the DC-DC converter of 1.52 volts, the supercapacitor was disconnected from the load and allowed to recharge once

it reached that level. It would then switch back to powering the device once it reached 4.6 volts. Using these equations, the results from the simulation were gathered and compared to the real-life test in the following graph.

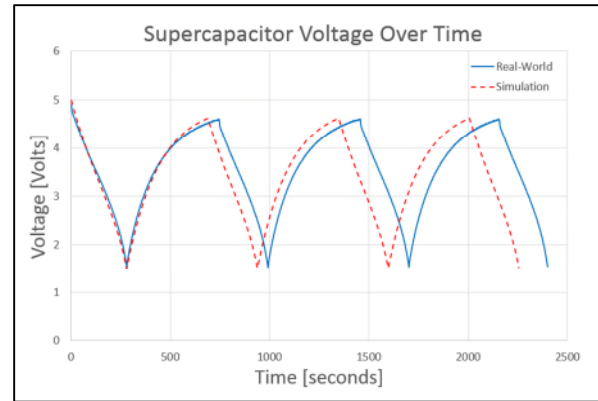


Figure 21. Real-World vs. Simulation comparison.

Figure 21 shows the voltage over time in the supercapacitor for both the real-world and the simulated test as it charges and discharges. Based on these results, the simulation was able to match the supercapacitors discharge profile with 98.9% accuracy while the charge profile predicts with an 89.5% degree of accuracy. In both instances the general shape of the charge/discharge curve looks good except when charging between around 4 and 4.5V, which also creates a net error in the predicted time constant that accumulates with each simulated cycle.

XII. CONCLUSION & FUTURE WORK

In this paper, a simulation tool that predicts the power lifetime of energy-harvested wireless sensor networks is presented. Based on the comparison between a real-world scenario and the simulation data, it can be seen that the software can predict the lifetime of a wireless sensor network with a high degree of accuracy. However, there is a noticeable margin of error in the results. This is likely to be due to a combination of reasons. Firstly, as mentioned, a Bluno V2 board was used to measure the voltage in the “Real-World” test, which had a margin of error of $\pm 0.15V$. Also, while the resistor was measured to be exactly 32.77Ohms, the capacitance of the supercapacitor was taken from the datasheet as the rated capacitance. Some simplifying assumptions were used for charging such as taking all the current from the resistor to be entering the supercapacitor when in reality a small percentage will go into the DC-DC converter, acting in quiescent/no load mode. Correspondingly, it is approximated that when the supercapacitor is discharging that all the source current for the DC-DC converter comes from the supercapacitor. However, over a given cycle these approximations should more or less ‘balance out’ but cause a small net approximation error.

With the implementation of a standardised way of characterising components, this simulation tool provides a much faster method for finding the optimum power setup for a particular application.

For future work, more in-depth analysis of the real-life charging and discharging currents should be undertaken via metrology and closer interaction with the supercapacitor vendor to understand device behaviour particularly in the 4-4.5V charging region. In particular the previously mentioned approximation error assumptions need to be validated and their magnitude assessed. The DC-DC converter will also be in ‘no load’ rather than quiescent operation so its characteristics in this mode need to be characterised. This should lead to more accurate calculations in future iterations of the model. The way that the software is setup allows for this, as each component has its own separate function, allowing for individual component improvements to the system as a whole. This tool could also be available online where every component added to the system can be available for everyone to use.

ACKNOWLEDGMENT

This work was part of a larger project titled ReCO2ST, (Residential Retrofit assessment platform and demonstrations for near zero energy and CO₂ emissions with optimum cost, health, comfort and environmental quality). This project has received funding from the European Union’s “Horizon 2020” research and innovation program under the grant agreement No. 768576.

REFERENCES

[1] SEAI. *Nearly Zero Energy Building Standard* [Online]. Available at: <https://www.seai.ie/sustainable-solutions/nearly-zero-energy-buildi-1/> [Accessed 11th June 2019].

[2] Statista. Internet of Things (IoT) connected devices installed base worldwide from 2015 to 2025 (in billions) [Online]. Available at: <https://www.statista.com/statistics/471264/iot-number-of-connected-devices-worldwide/> [Accessed 11th June 2019].

[3] EPA. *Sustainable Material Management* [Online]. Available at: <https://www.epa.gov/smm> [Accessed 5th June 2019].

[4] A. S. Weddell et al. Accurate Supercapacitor Modeling for Energy Harvesting Wireless Sensor Nodes. *Transactions on circuit and systems – II: Express Briefs*, 2011. [Online]. Volume 58, Issue 12, Pages 911-915. Available at: <https://ieeexplore.ieee.org/document/6093951> [Accessed 13th May 2019].

[5] C. Hsu et al. An effective Seebeck coefficient obtained by experimental results of a thermoelectric generator module. *Applied Energy* [Online]. Volume 88, Issue 12, Pages 5173-5179, 2011. Available at: <https://www.sciencedirect.com/science/article/pii/S0306261911004788#s0010> [Accessed 21st May 2019].

[6] L. Mentally, A. Amghar, H. Sahseh. Comparison between HC, FOCV and TG MPPT algorithms for PV solar systems using buck converter, 2017. [Online]. 2017 International Conference on Wireless Technologies, Embedded and Intelligent Systems (WITS). Available at: <https://ieeexplore.ieee.org/document/7934609> [Accessed 6th June 2019].

[7] J. Ahmad. A Fractional Open Circuit Voltage Based Maximum Power Point Tracker for Photovoltaic Arrays, 2010. [Online]. 2010 2nd International Conference on Software Technology and Engineering. Available at: <https://ieeexplore.ieee.org/document/5608868> [Accessed 10th June 2019].

[8] D. Baimel, S. Tapuchi, Y. Levron, and J. Belikov, "Improved Fractional Open Circuit Voltage MPPT Methods for PV Systems," *Electronics*, vol. 8, no. 321, 2019.

Reducing The Energy Consumed During Multihop Transmissions in Wireless Sensor Networks

Anne-Lena Kampen

Western Norway University of Applied Sciences
Bergen, Norway
e-mail: alk@hvl.no

Knut Øvsthus

Western Norway University of Applied Sciences
Bergen, Norway
e-mail: kovs@hvl.no

Abstract—Reducing energy consumption in Wireless Sensor Networks (WSN) is important in order to lengthen the network lifetime and reduce maintenance cost. Although its substantial contribution, the energy consumed to overhear is often omitted in energy calculations. However, here it is included to model the tradeoff between the expected number of transmissions, transmission range, number of hops, and overhearing, to discover the optimal distance between the nodes along the routing path. Our calculations show that to reduce energy consumption, the node should choose their successors close enough to prevent the expected number of transmissions from exceeding 1.4. The access protocol is Low Power Listening (LPL), and we also present a solution to reduce the energy consumption of the nodes that are crucial for maintaining an operational network, i.e., the nodes whose successor is the sink.

Keywords—WSN; Energy; LPL; Energy-Modelling; Multi-Hop; Overhearing

I. INTRODUCTION

Wireless Sensor Networks (WSN) [1] are used in a wide range of areas from industrial applications [2] and smart grid [3][4] to healthcare [5], and used in all type of environments, from rural to urban areas [6]. The WSNs consist of sensor nodes that monitor their surroundings' characteristics and relay collected information to a common central, generally called the sink. The network has several advantages such as flexibility, lack of wiring, and autonomous operation.

One of the main issues related to WSN is energy consumption. The nodes constituting a WSN are generally low-cost battery-powered devices with limited energy capacity. Hence, reducing energy consumption is essential in order to extend the individual nodes' lifetime, and maintain a well-functioning network [7]. The radio is the primary energy consumer [8][9]. During operation, the radio switches between various states such as receiving, transmission, idle and sleep, all of which consume different amounts of energy [4]. To save energy, the nodes should remain in the sleep state whenever possible. One of the most frequently cited energy-reducing approaches is the Low-Power-Listening (LPL) protocol [10][11], where nodes wake up periodically to sense the channel. To ensure successful data exchange, the senders transmit a preamble message to signal upcoming data transmission. The duration of the preamble must be long enough to ensure that the intended receiver hears it. This paper investigates further energy-reducing measures in networks running LPL.

The total energy that is consumed to transmit data from a source to sink depends on several factors. First, all the nodes use energy to send their own generated data. Second, nodes along the routing path consume energy to receive and forward data. Third, overhearing nodes consume energy when they receive packets, which they afterward discard. These are the nodes located in the proximity of the path such that they are covered by the transmissions intended for different destinations. Forth, energy is wasted when packets fail to reach the sink and must be retransmitted. One of the factors that impact the packet delivery success is the distances between the successive nodes along the routing path. Successful packet delivery is likely when the distance is well within the transmission range. As the distance increases, the probability of success reduces until it gets unlikely as the distance increases beyond the transmission range. Thus, to maintain a high probability for successful delivery, the distance between the nodes along the path should be shorter than the transmission range. However, short distance means that the number of hops to reach the sink increases. Each hop increases the number of nodes that play an active part in forwarding the packet, increasing energy consumption. Another approach is, therefore, to increase the nodes' transmission range. However, such a solution requires that each node along the path increases the output power, increasing energy consumption. Thus, there is an energy-tradeoff between packet delivery-success, transmission range, and hop count. This paper investigates this energy-tradeoff.

As well as minimizing the total energy consumed, it is important to balance the workload in the network to avoid early depletion of nodes. Depleted nodes cannot provide their own sensed data, and, as a more serious consequence they may lead to network partitioning. As data in WSNs are generally directed toward the sink, there is an innate energy imbalance in WSNs. That is, nodes in the proximity of the sink must forward data from nodes located further away such that the forwarding load increases with decreasing hop-count. Thus, the one-hop nodes deplete energy faster since they undergo the heaviest forwarding load. In addition, they are the most critical to keep the network connected.

To alleviate this imbalance, we suggest to reduce the one-hop nodes energy consumption by preventing them from transmitting the preamble. Remember, the preamble transmission is used to wake up and prepare the intended receivers to read the upcoming data packet. However, the sink is always awake and ready to receive.

The contribution of this paper is to investigate the tradeoff between the number of re-transmissions, transmission range, the number of overhearing nodes, and number of hops in WSN to discover an energy optimal distance between the consecutive nodes along the path. In addition, we suggest a simple approach to reduce energy consumption in networks running LPL. The scheme is verified by simulations, and shows that energy consumption is substantially reduced.

The rest of the paper is organized as follows. Section 2 presents related works. Section 3 presents the energy model for one-hop transmission, while Section 4 presents the model for multihop transmission. The energy optimal transmission range is calculated in Section 5. Section 6 presents a model to calculate the energy consumed for nodes at various hop-counts, followed by an approach to reduce the one-hop nodes' energy consumption in Section 7. Section 8 presents the conclusion.

II. RELATED WORK

In order to develop energy-efficient solutions for WSN, it is essential to understand the energy consumption of the individual nodes. Modelling of the energy-consuming activity provides valuable insight into this aspect.

The energy consumed is proportional to the time the nodes spend in the active state to transmit and receive. As the controller of the various radio states [12], the MAC protocol is important to reduce energy usage. A common MAC layer method to save energy is to switch to the sleep state whenever possible [13]. However, to keep a WSN network connected and operational, the nodes must periodically switch to the active state. During the active periods, the nodes listen for transmissions, and they may exchange synchronization information [14]. The energy consumed for such periodic wakeups is included in the model presented in [15], which calculates the energy consumption for communication, acquisition, and processing. The model is used to illustrate how energy is reduced with a reduced number of active periods. A solution to reduce the need for periodic listening is to apply always-on wakeup radios with very low power consumption [16]. The always-on radio activates the central part of the nodes only when it detects activity on the medium. Although an interesting solution, it will not reduce the number of overheard transmissions, and the solution makes the nodes more complex.

Several models for energy consumption in WSN are found in the literature. A stochastic model that estimates the expected energy consumed, and the expected lifetime of WSN nodes, is presented in [17]. The model is based on the time the nodes spend in various states such as sleeping, sensing, and relay. The communication is based on CSMA/CA. The deterministic energy bounds associated with maximum and minimum energy consumption are presented in the paper. In [18], a framework for modelling MAC protocols is presented. The framework can be used for energy calculations that are based on an absorbing Markov chain analysis. An analytical energy model that demonstrates the impact of the various parts of the PHY and MAC layer, is presented in [19]. A receiver-initiated communication protocol is used, where the receivers periodically wake-up and transmit a wakeup beacon to signal

that they are ready to receive. Testbed measurements that isolate hardware and software consumption are performed to understand the energy consumption and validate the model. It shows a relative error of 8% compared to the real energy estimate. A common aspect of these models is the focus on MAC-related activities related to switching between different states.

An energy consumption model that also includes overhearing is presented in [20]. The energy consumption is modeled both for sender- and receiver-initiated asynchronous MAC protocols, as well as synchronous MAC protocols for multimedia sensor networks. They found that the receiver-initiated protocols generally outperform sender-initiated protocols, although LPL performs well under low sampling rates. A weakness of the calculations is that the LPL protocol modeled is very conservative, since only full preamble is considered.

Increased transmission range increases the senders' energy consumption. In addition, both the number of overhearing nodes and collision probability increase. The overhearing nodes waste energy to receive data addressed to neighboring nodes, and collisions require re-transmission. A number of analytical models are suggested to understand the energy impact of the transmission range. In [21], they use energy models to minimize the energy consumption of the nodes while meeting the delay constraints. The energy model suggested in [22] calculates the total energy consumed per successfully received bit. They study the tradeoff between energy per successfully received bit and the energy used for transmission. They find a single energy-optimal transmission range that is validated using real data. In [23], the energy consumption as a function of transmission range is modeled and used to balance the energy consumption among the nodes when new versions of programs are broadcasted throughout the network. Energy dissipation is modeled to study the impact of transmission power on both the data and the ACK packets in [24]. They assume a TDMA based communication model. When the data packets are much larger than the ACK packets, the latter should be sent with the highest possible output power to improve their delivery reliability. The reason is that higher output power increases the packet delivery-success probability.

There is an energy-tradeoff between transmission range, the number of overhearing nodes, and the number of hops between source and destination. Increased transmission range may decrease the number of transmissions and the number of hops toward the sink. However, the number of overhearing nodes, as well as the transmission energy consumption, increase. The hop count is considered in [25], where the transmission range is adjusted to balance the energy when transmitting data in multi-sink networks. In [26], overhearing is included, and the conclusion is that the transmission range should be short to reduce the number of overhearing nodes and reduce the collisions probability. In contrast, twelve reasons for having a long transmission range are listed in [27]. One of the main reasons listed is that a longer transmission range makes the routing path closer to the Euclidian distance. However, overhearing would be a limiting factor since receiving consumes energy in the same order of magnitude as

transmitting in WSN. In this paper, we investigate the effect of reducing overhearing. In addition, we take loss probability and routing distance to sink into consideration.

III. ENERGY MODEL FOR ONE-HOP TRANSMISSION

In this section, the energy consumed during one-hop transmission is modeled. The communication protocol applied is LPL, which is a preamble-based protocol where nodes periodically wake up to listen for activity [10][11][28]. Between the wakeup periods, the nodes remain in sleep mode. A preamble message is used to inform the neighboring nodes to stay awake to receive the message that is about to be sent. Its length is defined by the nodes with the longest sleep period to ensure that all nodes are informed. Upon receiving a preamble, the node remains active, listening for the rest of the preamble and the upcoming message.

Assuming that the sleeping time of the nodes is approximately equal, the nodes will, on average receive half of the preamble. For all the nodes except the intended receiver, this is a waste of energy. In order to reduce the energy consumed to receive the preamble, the preamble can be divided into small preamble-fractions containing the receiver's address and the start-time for the data-packet transmission [29]. In this way, the overhearing nodes can enter sleep mode after receiving a preamble-fraction. In addition, the intended receiver is no longer required to stay awake to receive the whole preamble. Rather, it can receive a fraction and then enter sleep mode until data transmission. We call this method divided-preamble.

To model the energy consumption, we assume a network that uses divided-preamble LPL. Figure 1 illustrates packet transmission for such a network. We assume that there are four nodes, named N1, N2, N3, and N4, which all hear each other's transmissions. The red squares represent a data-packet that is sent from node N1 to N3. The dark blue squares represent the preamble, which is sent just before the associated data-packets. The duration of one complete preamble is p . Note that divided-preamble is used, thus the blue preamble squares are divided into fractions of length Δp . The preamble must be long enough to ensure that each node wakes up and listens for activity at least once per preamble. Otherwise, they may lose a preamble transmission. The light blue shaded squares are the time periods when the nodes are in sleep mode. The periodic, green squares, named L_T , are the time when nodes listen for activity. Hence, L_T must appear at least once per period p . The orange squares illustrate that the nodes received and read one of the preamble-fractions. Only the receiver wakes up to receive the data-packet, illustrated by the red square on node N3's timeline.

The nodes affected by one-hop transmission are the transmitting and receiving node, and the nodes overhearing the transmission. The transmission time for the packet is b . The power consumed for transmission consists of a fixed part, k_1 , plus an offset, k_2 , that is proportional to the radiated power [23][30]. The transmission range is d . A preamble, p , is transmitted prior to each data-packet, b . Thus, the energy consumption for transmission is $(k_1+k_2d^2) \cdot (b+p)$, represented by the first term in our model in (1). The second term in (1) calculates the energy consumed by the intended receiver as it

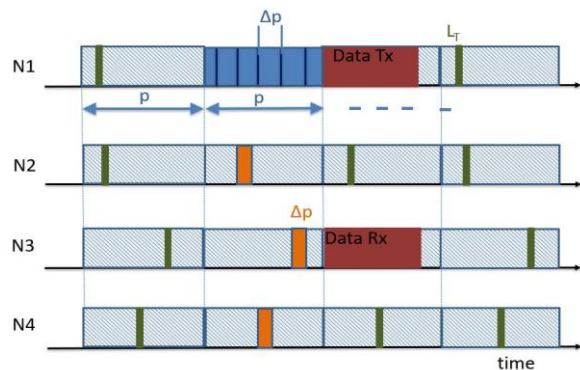


Figure 1. Packet transmission and reception in LPL using divided-preamble.

receives the data packet. Receiving and listening consume a fixed amount of power, k_3 . The preamble-fraction has a time duration Δp . It contains the receiver's address and the start-time for packet transmission. We assume that Δp includes both the preamble-fraction and the small interframe spacing between the fractions. The node density is λ . Thus, the number of nodes covered by the transmission is $\lambda \cdot \pi d^2$. On the average, all nodes covered by the transmission receive $1.5 \cdot \Delta p$. The reason is that the nodes must receive a whole preamble-fraction but they wake up at a random time. That is, it is equally likely that a node wakes up at any point during the preamble-fraction transmission. However, it must receive the complete preamble-fraction to be able to read its content. Thus, if a node wakes up after transmission of a preamble-fraction has started, it must remain in the receiving state until it receives the subsequent complete preamble-fraction. The nodes will, therefore, on average, receive one half preamble-fraction in addition to the complete fraction that it is able to read. The energy consumed is represented by the last term in (1). The number of overhearing nodes is calculated based on the node density, the transmitting node is accounted for by subtracting one. Thus, the energy that is consumed per one-hop communication is:

$$E = (k_1 + k_2 d^2)(b + p) + k_3 b + 1.5 \Delta p (k_3 \pi \lambda d^2 - 1) \quad (1)$$

IV. ENERGY MODEL CONSIDERING MULTIHOP COMMUNICATION AND LOSS PROBABILITY

Our focus is the energy consumed during data forwarding from source to sink. The goal is to investigate the impact that both overhearing, transmission range and re-transmission have on the energy optimal transmission range. Short transmission ranges increase the number of hops between source and destination, increasing the number of transmissions, thus also the total number of re-transmissions is likely to increase. Re-transmissions increase energy consumption. Increasing the transmission range reduces the number of hops. The disadvantage is the increasing transmission energy consumption, and the number of

TABLE 1 LIST OF PARAMETERS AND ACRONYMS

Symbol	Meaning
k_1	Energy consumed to transmit, fixed part
k_2	Energy consumed to transmit, proportional to radiated power
k_3	Energy consumed to receive
λ	Node density
d	Transmission range
p	Preamble
b	Data packet
Δp	Preamble-fraction
q	Packet loss rate
x	Distance between communicating nodes
x_0	Knee value
x_1	Border area width
N	Number of nodes along a path
m	Number of transmission trials
D	Distance to sink
h	Hop-count distance to the sink
n_h	Number of nodes at hop distance h
$T_{x_{n_h}}$	Number of transmissions for a node at hop-count n_h
ETX	Expected number of transmissions
PDR	Packet delivery rate
SD	Successor distance factor, $x = x_0 \cdot SD$

overhearing nodes increases due to a larger area covered by each transmission. The impact of the overhearing nodes is determined by how much of the transmission is being overheard.

A receiver experiences increasing re-transmissions when it is located at the border area of the sender's transmission range [31]. We use the model presented in [32] to define the border area. The model is used to create the graph on the left-hand side of Figure 2, where the x-axis represents the distance between the sender and the receiver. The y-axis represents the Packet Delivery Rate (PDR). In the figure, the transmission range is approximately 10 m. The PDR equals 1 when the distance between the sender and the receiver is much shorter than the transmission range. However, at distances in the vicinity of the transmission range, there is a transient area where the PDR starts to change and bends towards zero. This is the border area. The distance between a transmitter and its border area increases with increasing transmission power. Hence, the number of re-transmissions can be reduced by increasing the transmission energy.

Based on the border-area discussion above, the total number of re-transmissions along the path from source to sink depends on the nodes' transmission range and the associated hop-to-hop distance, i.e., the distance between the transmitting node and its successor. Assuming equal

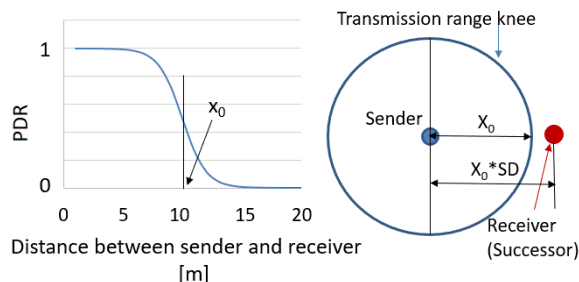


Figure 2. The left-hand side of the figure shows the PDR for increasing distance between sender and receiver. The small blue circle in the center of the right-hand side figure illustrates a transmitting node, and the blue outer circle is the knee-point border line for the transmission.

transmission power and hop distances, the expected number of transmissions (ETX) along a path is [31] found to be:

$$ETX[N] = \frac{1-q^m - (1-q^m)^N}{q^m(1-q)} \quad (2)$$

N is the number of nodes along the path, which is equal to the distance to the sink, D , divided by transmission range, d . The factor m denotes the maximum number of transmission trials, i.e., the maximum number of re-transmissions is $(m-1)$. The parameter named q , denotes the packet loss rate. $q = 1 - PDR$, and $PDR(x)$ is given by [32]:

$$PDR(x) = \frac{1}{1 + e^{-x/x_1}} \quad (3)$$

x is the distance between the transmitting node and its successor, and x_1 defines the width of the border area. x_0 is in the middle of the border area, i.e., x_0 is the knee value as shown in Figure 2. The expected number of transmissions along a path, $ETX[N]$, depends on the packet loss rate q . The energy consumed for transmitting a packet from source to sink can be found by introducing $ETX[N]$ in (1):

$$E = ETX[N] [(k_1 + k_2 d^2)(b + p) + k_3 b + 1.5 \Delta p (k_3 \pi \lambda d^2 - 1)] \quad (4)$$

Equation (4) shows that $ETX[N]$ has an important impact on energy consumption. $ETX[N]$ increases both with the number of hops along the path toward the sink, and when the distance between sender and successor nodes approaches and enters the border area. The distance to x_0 can be increased by increasing the transmission power, thus the tradeoff between hop-count, packet delivery rate (here represented by ETX), overhearing, and transmission range. The tradeoff is investigated in the next section.

V. ENERGY OPTIMAL TRANSMISSION

We use (4) to investigate the tradeoff between hop-count, packet delivery rate, overhearing, and transmission range. It is assumed to be an equal distance between the sender and the receiver for each hop along the path from the source node to the sink. The right-hand side of Figure 2 illustrates the sender-receiver distance for one of these individual hops along the path. The blue node represents one sender, and the blue circle represents the associated knee-point value, x_0 , for the sender's transmission range. The red dot represents a receiver at a distance to the sender, its distance is outside the knee-point value. In order to model this sender-receiver distance, we choose to represent it as the knee-point value times a constant. The constant is named Successor Distance factor (SD), i.e., $x = x_0 \cdot SD$. Hence, the red node has SD higher than 1. A node located on the blue circle will have $SD = 1$ and a node located inside the blue circle would have a SD lower than 1.

The parameter values used in the calculations are the values presented in [30]. The values are based on the CC1000_radio [33]. For CC1000, k_3 and k_2 are in the same order of magnitude while k_2 is much lower than k_3 . Other radios may have different numerical values. However, the

characteristics are similar among WSN nodes [8][23]. Hence, our calculations present a general trend. The values for k_1 , k_2 and k_3 are $36.1\mu\text{J/bit}$, 0.06 pJ/bit/m^2 and $37.5\ \mu\text{J/bit}$ respectively. The preamble-time, p , is normalized with respect to data-packet time, b . The transmission range $d = 10\text{m}$ and the node density $\lambda = 0.015$. The preamble-length is 5-data-packet length. The distance to the sink is set to $D = 50\text{m}$ and the maximum number of re-transmissions is $m = 20$.

In the calculations, the successor node is located at $x = x_0 \cdot \text{SD}$. Thus, the number of nodes along a path is $N = \text{round-up-upward}(D/x)$. Calculating energy consumed the overhearing nodes is challenging. The reason is that some are located inside x_0 , but do not receive the preamble or are not able to correctly decode the preamble. The same apply for some of the nodes that are located in the border area beyond x_0 . As an average, assume that all nodes inside x_0 receive the preamble.

Figure 3 shows the energy consumption changes as transmission range increases. The y-axis represents the energy consumption and the x-axis represents the transmission range knee value, x_0 . That is, moving toward higher x-axis values, the transmission power increases, and thus the transmission range. ETXper-hop changes with transmission range and is calculated using equations presented in [32], see reference for explanation: $\text{ETX}(m) = (1-q^m)/(1-q)$. The figure shows three different graphs representing three different SD parameters. For the blue graph $\text{SD} = 0.5$ ($\text{ETXper-hop} = 1.19$), for the orange graph the $\text{SD} = 0.75$ ($\text{ETXper-hop} = 1.43$) and for the yellow graph $\text{SD} = 1.25$ ($\text{ETXper-hop} = 3.3$).

First, we concentrate on the impact of SD distance. The smallest SD, the blue graph, generally gives the highest consumption. The reason is that low SD gives short hop-to-hop distances such that the number of hops from source to sink is high. Remember, each hop adds at least one packet transmission, causing energy to increase due to transmission, receiving, and overhearing. When SD increases, the hop-count decreases, reducing the energy consumed. However, as the SD is further increased, the increase in $\text{ETX}[N]$ cancels the positive effect of the reduced number of hops, because the successor is too far into the border area. The energy consumption for $\text{SD} = 1.25$ is generally higher than for $\text{SD} =$

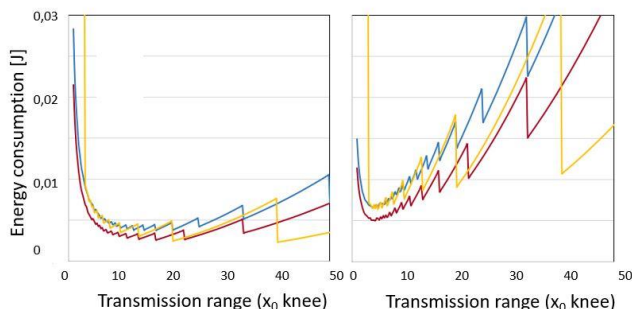


Figure 3. Energy consumption related to transmission range. The left-hand side of the figure shows the energy consumed when the preamble-fraction that overhearing nodes receive is 0.1 times the complete preamble. The figure on the right-hand side shows the results when overhearing nodes receive 0.5 times the complete preamble.

0.75 although the hop-count for $\text{SD} = 1.25$ is the lowest due to the long sender-to-receiver distance. Performing the calculations with various SD shows that energy consumption is lowest when SD is about 0.75 ($\text{ETXper-hop} = 1.4$). That is, the successor nodes should be chosen so far into the border area that the $\text{ETXper-hop} = 1.4$. The result is comparable to the discussions and findings in [10], where energy minimization for LPL in noisy environments is investigated. It is found that noise-triggered false wakeups can be a dominant energy consumption factor. In our case, overhearing causes unnecessary wakeups, which does not provide any valuable information, thus it should be limited.

Furthermore, Figure 3 shows that there exists an energy optimal transmission range. It is mainly determined by the overhearing nodes' energy consumption. The optimal transmission range is more pronounced and shorter as Δp (fraction of preamble received by neighboring nodes) increases. The graph to the right in Figure 3 has the highest Δp and the shortest and most pronounced optimal transmission range. The reason is that increased Δp causes increased energy consumption among overhearing nodes, because they receive a larger fraction of the transmitted preamble. Combined with the fact that the number of overhearing nodes increases quadratic with distance, the energy optimal transmission range is reduced to reduce the impact of overhearing. When Δp is low, the optimal transmission range is less pronounced and longer because the impact of overhearing is much lower. The optimal transmission range is about 10m for $\lambda = 0.015$. Thus, the average number of nodes covered by the transmission is 4.71, which may be too few to keep the network connected [34]. The conclusion is that it is energy efficient to keep the transmission range short, considering that the range is long enough to keep the network connected. Other parameter values would give other results. For instance, there is no pronounced energy optimal transmission range if Δp is reduced to below 0.02 while the other parameters are kept unchanged. Reducing the preamble, p , to data-packet size has the same effect of making the optimum-point less pronounced. On the contrary, increasing the node density makes it more pronounced. However, the energy optimal distance, between a node and its successor, is the distance where ETXper-hop is 1.4. This applies for all the various parameter settings. Deciding a distance that gives $\text{ETXper-hop} = 1.4$ is not realistic in real-world scenarios since environmental characteristics are prone both to temporal and spatial changes. In addition, the parameter settings both for the radio as well as other parameters such as packet size would vary, resulting in a slightly different optimal ETXper-hop . However, our result shows a valid trend, the optimal distance between successor nodes should not be too far into the border area, i.e., the area where the PDR starts to change and bends towards zero.

We observe a sawtooth shape of the curves in Figure 3. The reason for this shape is that the number of overhearing nodes increases, initially, with increasing transmission range, as seen in the smooth increasing energy consumption. The abrupt drop occurs as the path decreases by one link. The reduced number of hops gives a sharp reduction in overhearing energy consumption since the number of

transmissions is reduced. The deepest sawtooth decrease in energy consumption occurs for the longest transmission ranges. The reason is that the longest transmission range covers the highest number of overhearing nodes.

VI. ENERGY BALANCE IN WSN

Although LPL is an efficient method to reduce the energy consumption in WSN, there is an energy imbalance in energy consumption among the nodes. The energy consumption due to forwarding increases towards the sink. The reason is that nodes closer to the sink must forward packets from nodes further away from the sink. The consequence is that the one-hop nodes experience the highest energy-cost due to their packet forwarding.

To investigate energy consumption versus hop-count, we assume a fair workload balance between the nodes. Fair means equal load-balanced among the nodes at a given hop-count. Assume that the nodes' transmission range is d and h represent the hop-count distance to the sink. The number of nodes located $(h+1)$ hops from the sink is equal to the number of nodes inside the donut-shaped area with an outer radius of $d \cdot (h+1)$ and an inner radius of $d \cdot h$. The number of nodes in the donut-shaped-area is found by multiplying its area with the node density, λ :

$$n_{h+1} = \pi\lambda \left[((h+1) \cdot d)^2 - (hd)^2 \right] = \pi\lambda(2h+1)d^2 \quad (5)$$

The number of nodes located $h+2$ hop from the sink is:

$$\begin{aligned} n_{h+2} &= \pi\lambda \left[((h+2)d)^2 - ((h+1)d)^2 \right] \\ &= \pi\lambda(2h+3)d^2 \end{aligned} \quad (6)$$

Nodes at hop-count h forwards data on behalf of a given number of nodes at hop-count $h+1$. The average number of nodes use a given node at hop-count h is:

$$\frac{n_{h+2}}{n_{h+1}} = \frac{2h+3}{2h+1} \quad (7)$$

A node at hop-count h transmits one of its packets, in addition, it transmits $(n_{h+1})/(n_h)$ packets from its one-hop predecessors. The total number of transmissions for a node at hop-count n_h is, therefore:

$$Tx_{nh} = 1 + \frac{n_{h+2}}{n_{h+1}} \cdot Tx_{n(h+1)} \quad (8)$$

Based on (8), we find the energy consumed for nodes at a given hop-count is presented in (9). The first term in (9) represents the transmission energy. The second term represents the energy used to receive packets for forwarding, remember, the preamble is received for each received data-packet. Besides, the nodes overhear neighbors' transmissions. Some of the overheard neighbors are located at the same hop-count distances from the sink as the overhearing node, while some are located at adjacent hop-count distances. Assuming that the contribution from all these three hop-count distances

is equal, the number of transmissions overheard is as expressed in the first parenthesis of the last term in (9). However, each packet is received twice for nearby neighbors: once when the neighbor receives it, once when the neighbor transmits it. Other neighbors' packets are overheard only once: when the neighbor transmits it. As a first approximation, we assume that half of each overheard packet is received twice, hence, the 1.5-factor in front of the parenthesis in (9). Thus, to investigate the energy imbalance, the energy consumed for a node at hop-count x can be calculated as:

$$\begin{aligned} E &= Tx_{nh} [(k_1 + k_2 d^2)(b + p)] + k_3 (Tx_{nh} - 1) \cdot \\ &(b + 1.5\Delta p) + 1.5 \left(\frac{Tx_{nx-1} + Tx_{nx} + Tx_{nx+1}}{3} \right) (k_3 1.5\Delta p) \end{aligned} \quad (9)$$

VII. BALANCING ENERGY CONSUMPTION

Although LPL is an efficient energy reduction method in WSN, the energy imbalance persists among the nodes. Caused by the forwarding load discussed above, the one-hop nodes consume much more energy than the other nodes. However, messages sent from the one-hop nodes are destined to the sink, which is always active. Therefore, in order to save energy, we suggest canceling the preamble from the one-hop nodes. The nodes are aware of their identity as one-hop nodes by looking in the routing table: their successor nodes are the sink, and their distance to the sink is one hop.

Simulations are performed to compare when all nodes apply the same divided-preamble LPL algorithm against the case when the one-hop nodes are prevented from transmitting the preamble. The parameter investigated is total energy consumption. The simulation is performed in Omnet++ [35].

The applied routing metric is hop-count, and each node generates 100 data packets during each simulation. The preamble time is four times the duration of a data packet. The preamble-fraction packets are one-tenth of the data-packet size. We have used a fixed number for receiving power consumption. The transmission power consumption is also fixed since the transmission range is equal for all nodes. Energy consumed for overhearing is not considered because the number of overhearing packets would be equal for both scenarios: The number of packets transmitted is equal for approaches, and, although the one-hop nodes do not transmit preamble, neighbors must receive and read all overheard packets in order to decide whether the packet is destined for them. 205 nodes are randomly distributed in an area of 1000 m times 1000 m. The transmission range of all nodes is 141 m.

The simulation results are shown on the left-hand side of Figure 4. Every simulation point presented in the graphs represents the average value of 100 simulation runs with different seeds for random deployment of nodes. The red curve shows the simulation result when the one-hop nodes are prevented from transmitting preamble, while the blue curve shows the energy consumed when the one-hop nodes behave equal to the other nodes, i.e., transmit preamble. The continuous curves represent average values, and the marks over and below represent the 95% confidence interval.

The simulations show that one-hop nodes' energy consumption is reduced by about 50% when the one-hop nodes are prevented from transmitting the preamble. Calculations using (9) verify the simulated result, as shown on the figure's right-hand side. To what extent the energy is reduced depends on various factors, the main being the ratio of preamble size to data-packet size. Less energy is saved when the preamble is shorter. For instance, the energy saving is reduced to 19% if the preamble to data-packet-size is reduced to 0.5. Avoiding preamble transmission would reduce one-hop nodes' energy consumption, which are the most critical nodes to keep the network connected. Preventing transmission of the preamble is equal to reducing the duty-cycle of the nodes, and our result complies with the results in [36], where duty cycling is used to manage the delay as well as energy consumption of the nodes. The duty-cycle of the hot-spot nodes, which equals to the one-hop nodes, is kept low compared to the duty-cycle of nodes in non-hotspots areas.

VIII. CONCLUSION

To reduce the energy consumed in multihop transmission in WSN the tradeoff between number of re-transmissions, overhearing, number of hops, and transmission range are investigated. Due to improved packet delivery rate (PDR), less energy is wasted on re-transmissions when the distance between senders and receivers along the routing paths is reduced. However, the number of hops to reach the sink is increased such that more nodes must use energy to forward the data. Another solution is to increase the nodes' output power to increase the distance to where the PDR starts to fail. In this way, the distance between senders and receivers can increase without introducing more re-transmissions. However, each transmission consumes more energy. In addition, the overhearing nodes must be considered. Their contribution to energy consumption increases with the number of nodes covered by the transmissions, number of transmissions, and the size of the received packet. Investigating the tradeoff between all mentioned factors, we find that the optimal solution is for the nodes to choose their successors at a distance that gives an expected number of transmissions, ETXper-hop, of approximately 1.4. In addition, we suggest and show that energy is efficiently reduced if nodes whose successor is the sink, are prevented from transmitting preamble. The preamble can be omitted since the sink is always awake and ready to receive. Reducing these nodes energy consumption is crucial in order to avoid network partitioning.

Future work on energy consumption in WSN will focus on more intelligent forwarding. Nodes will predict the traffic patterns to optimize their own duty-cycle and prevent overhearing.

REFERENCES

[1] S. J. Ramson and D. J. Moni, "Applications of wireless sensor networks—A survey," in 2017 International Conference on Innovations in Electrical, Electronics, Instrumentation and Media Technology (ICEEIMT), 2017: IEEE, pp. 325-329.

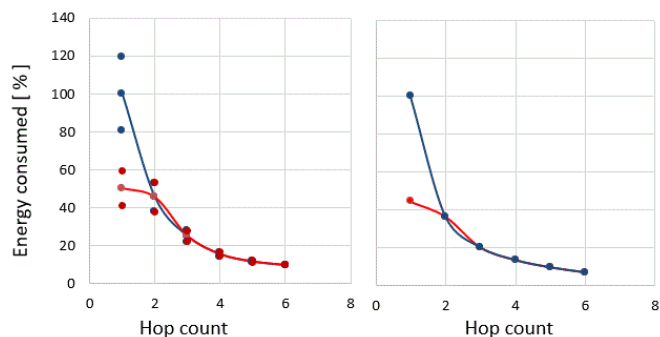


Figure 4. Energy consumption for nodes at different hop-count distances from the sink. The graphs on the right-hand side show calculated results. The graphs on the left-hand side show simulated results.

[2] X. Li, et al. , "A review of industrial wireless networks in the context of Industry 4.0," *Wireless networks*, vol. 23, no. 1, pp. 23-41, 2017.

[3] M. Erol-Kantarci and H. T. Mouftah, "Wireless sensor networks for cost-efficient residential energy management in the smart grid," *IEEE Transactions on Smart Grid*, vol. 2, no. 2, pp. 314-325, 2011.

[4] R. W. R. de Souza, L. R. Moreira, J. J. Rodrigues, R. R. Moreira, and V. H. C. de Albuquerque, "Deploying wireless sensor networks-based smart grid for smart meters monitoring and control," *International Journal of Communication Systems*, vol. 31, no. 10, p. e3557, 2018.

[5] N. Dey, A. S. Ashour, F. Shi, S. J. Fong, and R. S. Sherratt, "Developing residential wireless sensor networks for ECG healthcare monitoring," *IEEE Transactions on Consumer Electronics*, vol. 63, no. 4, pp. 442-449, 2017.

[6] B. Rashid and M. H. Rehmani, "Applications of wireless sensor networks for urban areas: A survey," *Journal of network and computer applications*, vol. 60, pp. 192-219, 2016.

[7] H. Yetgin, K. T. K. Cheung, M. El-Hajjar, and L. H. Hanzo, "A survey of network lifetime maximization techniques in wireless sensor networks," *IEEE Communications Surveys & Tutorials*, vol. 19, no. 2, pp. 828-854, 2017.

[8] Đ. Bandur, B. Jakšić, M. Bandur, and S. Jović, "An analysis of energy efficiency in Wireless Sensor Networks (WSNs) applied in smart agriculture," *Computers and electronics in agriculture*, vol. 156, pp. 500-507, 2019.

[9] P. Dutta, J. Taneja, J. Jeong, X. Jiang, and D. Culler, "A building block approach to sensornet systems," in *Proceedings of the 6th ACM conference on Embedded network sensor systems*, 2008, pp. 267-280.

[10] T. Dinh, Y. Kim, T. Gu, and A. V. Vasilakos, "An adaptive low-power listening protocol for wireless sensor networks in noisy environments," *IEEE systems journal*, vol. 12, no. 3, pp. 2162-2173, 2017.

[11] R. C. Carrano, D. Passos, L. C. Magalhaes, and C. V. Albuquerque, "Survey and taxonomy of duty cycling mechanisms in wireless sensor networks," *IEEE Communications Surveys & Tutorials*, vol. 16, no. 1, pp. 181-194, 2013.

[12] V. L. Quintero, C. Estevez, M. E. Orchard, and A. Pérez, "Improvements of energy-efficient techniques in WSNs: a MAC-protocol approach," *IEEE Communications Surveys & Tutorials*, vol. 21, no. 2, pp. 1188-1208, 2018.

[13] H. Mostafaei, A. Montieri, V. Persico, and A. Pescapé, "A sleep scheduling approach based on learning automata for WSN partialcoverage," *Journal of Network and Computer Applications*, vol. 80, pp. 67-78, 2017.

- [14] A. Kumar, M. Zhao, K.-J. Wong, Y. L. Guan, and P. H. J. Chong, "A comprehensive study of iot and wsn mac protocols: Research issues, challenges and opportunities," *IEEE Access*, vol. 6, pp. 76228-76262, 2018.
- [15] B. Martinez, M. Monton, I. Vilajosana, and J. D. Prades, "The power of models: Modeling power consumption for IoT devices," *IEEE Sensors Journal*, vol. 15, no. 10, pp. 5777-5789, 2015.
- [16] A. Kozłowski and J. Sosnowski, "Energy efficiency trade-off between duty-cycling and wake-up radio techniques in IoT networks," *Wireless Personal Communications*, vol. 107, no. 4, pp. 1951-1971, 2019.
- [17] V. Agarwal, R. A. DeCarlo, and L. H. Tsoukalas, "Modeling energy consumption and lifetime of a wireless sensor node operating on a contention-based MAC protocol," *IEEE Sensors Journal*, vol. 17, no. 16, pp. 5153-5168, 2017.
- [18] F. A. Aoudia, M. Gautier, M. Magno, O. Berder, and L. Benini, "A generic framework for modeling MAC protocols in wireless sensor networks," *IEEE/ACM Transactions on Networking*, vol. 25, no. 3, pp. 1489-1500, 2016.
- [19] M. Alam, O. Berder, D. Menard, T. Anger, and O. Sentieys, "A hybrid model for accurate energy analysis of WSN nodes," *EURASIP Journal on Embedded Systems*, vol. 2011, pp. 1-16, 2011.
- [20] T. AlSkaif, B. Bellalta, M. G. Zapata, and J. M. B. Ordinas, "Energy efficiency of MAC protocols in low data rate wireless multimedia sensor networks: A comparative study," *Ad Hoc Networks*, vol. 56, pp. 141-157, 2017.
- [21] Z. Fan, S. Bai, S. Wang, and T. He, "Delay-bounded transmission power control for low-duty-cycle sensor networks," *IEEE Transactions on Wireless Communications*, vol. 14, no. 6, pp. 3157-3170, 2015.
- [22] M. Abo-Zahhad, M. Farrag, and A. Ali, "Modeling and minimization of energy consumption in wireless sensor networks," in *2015 IEEE International Conference on Electronics, Circuits, and Systems (ICECS)*, 2015: IEEE, pp. 697-700.
- [23] Z. Chen, et al. , "Energy-efficient broadcasting scheme for smart industrial wireless sensor networks," *Mobile Information Systems*, vol. 2017, 2017.
- [24] H. U. Yildiz, B. Tavli, and H. Yanikomeroğlu, "Transmission power control for link-level handshaking in wireless sensor networks," *IEEE Sensors Journal*, vol. 16, no. 2, pp. 561-576, 2015.
- [25] S. Bing and Z. Yujing, "Energy efficiency in multi-sink linear sensor network with adjustable transmission range," in *2016 8th IEEE International Conference on Communication Software and Networks (ICCSN)*, 2016: IEEE, pp. 462-466.
- [26] D. P. Dallas and L. W. Hanlen, "Optimal transmission range and node degree for multi-hop routing in wireless sensor networks," in *Proceedings of the 4th ACM workshop on Performance monitoring and measurement of heterogeneous wireless and wired networks*, 2009: ACM, pp. 167-174.
- [27] M. Haenggi, "Twelve reasons not to route over many short hops," in *IEEE 60th Vehicular Technology Conference*, 2004. VTC2004-Fall. 2004, 2004, vol. 5: IEEE, pp. 3130-3134.
- [28] J. Polastre, J. Hill, and D. Culler, "Versatile low power media access for wireless sensor networks," in *Proceedings of the 2nd international conference on Embedded networked sensor systems*, 2004: ACM, pp. 95-107.
- [29] A. Bachir, D. Barthel, M. Heusse, and A. Duda, "Micro-frame preamble mac for multihop wireless sensor networks," in *Communications*, 2006. ICC'06. IEEE International Conference on, 2006, vol. 7: IEEE, pp. 3365-3370.
- [30] A.-L. Kampen, K. Ovsthus, L. Landmark, and O. Kure, "Energy Reduction in Wireless Sensor Networks by Switching Nodes to Sleep During Packet Forwarding," in *The Sixth International Conference on Sensor Technologies and Applications*, SENSORCOMM, 2012, pp. 189-195.
- [31] J. Zhao and R. Govindan, "Understanding packet delivery performance in dense wireless sensor networks," in *Proceedings of the 1st international conference on Embedded networked sensor systems*, 2003, pp. 1-13.
- [32] K. Øvsthus, E. Nilsen, A.-L. Kampen, and Ø. Kure, "Modelling the Optimal Link Length in Wireless Sensor Networks for Two Different Media Access Protocols," 2015.
- [33] Chipcon Products from Texas Instruments. <http://www.ti.com/lit/ds/symlink/cc1000.pdf> (accessed October, 2020).
- [34] A.-L. Kampen, K. Ovsthus, and Ø. Kure, "An analysis of the need for dedicated recovery methods and their applicability in wireless sensor networks running the routing protocol for low-power and lossy networks," in *The 8th International Conference on Sensor Technologies and Applications*, SENSORCOMM, 01/01 2014, pp. 121-129.
- [35] "OMNeT++ Discrete Event Simulator." <https://omnetpp.org/> (accessed October, 2020).
- [36] Y. Liu, et al., "DDC: Dynamic duty cycle for improving delay and energy efficiency in wireless sensor networks," *Journal of Network and Computer Applications*, vol. 131, pp. 16-27, 2019.

Inductive Communication and Localization Method for Wireless Sensors in Photobioreactors

David Demetz

UMIT - Private University for Health Sciences,
Medical Informatics and Technology
Hall in Tirol, Austria
Email: david.demetz@umit.at

Alexander Sutor

UMIT - Private University for Health Sciences,
Medical Informatics and Technology
Hall in Tirol, Austria
Email: alexander.sutor@umit.at

Abstract—A method for an inductive communication and localization system for wireless sensors in internally illuminated photobioreactors is presented here. The communication is implemented through an on-off switched hartley-oscillator where its inductance is used as transmitting coil for the wireless sensor data. As modulation technique, the on-off keying is used. The magnetic field of the transmitting coil is sensed from outside the reactor with special designed receivers in order to evaluate the magnetic field components of the transmitting coil in all three spatial directions at one position. This enables the localization of the transmitting coil and thus the localization of the wireless sensor. A prototype has been implemented and test measurements performed with a two receiver setup. Additionally simulations were performed in order to see the accuracy improvement of the localization by using more receivers.

Keywords—wireless sensors; inductive localization; inductive communication.

I. INTRODUCTION

We already presented a wireless internal illumination system for photobioreactors in past [1]. The internal illumination of photobioreactors is needed due to the low penetration depth of light in the reactor medium. This novel illumination system consists of small wireless, inductively powered luminous spheres called Wireless Light Emitters (WLEs). The fact that the WLEs have the same overall density as water enables them to float in the reactor medium. The external magnetic field used to power the WLEs is generated by field coils driven by a class-E amplifier. The frequency of the alternating field is 178 kHz. The archived flux density in the photobioreactor amounts to approx. $B = 1 \text{ mT}$ [1]–[3].

For a better control of the processes inside the reactor, a further step is the measurement of crucial parameters such as temperature, salinity or oxygen concentration using wireless traceable sensors. Currently used setups use fixed sensors where drill holes or other reactor modifications are needed to install them. Using wireless sensors, those modifications are no more needed. In a similar project [4] they presented battery powered wireless sensor-spheres for bioreactors, which transmit their measured values using the 433 MHz frequency band. The sensors in our project will be powered through the inductive link used to power the WLEs. The traceability enables a spatial resolution of the measured values. The communication link is implemented as a separate inductive link with a carrier frequency of 297 kHz and is therefore

1.66 times higher than the frequency of the power supply field. This is to avoid interferences caused by harmonics. The mathematical description of the magnetic dipole field is used to solve the traceability task. Thereby the magnetic field of the data transmitting coil is measured in order to calculate the transmitter position. We already presented the design of our transmitter in another publication [5]. Now, we will take a closer look at the traceability task and the receiver design.

In Section II the chosen data transmission method and the used modulation technique are described. The model equations used to describe the magnetic field of a coil in order to derive the equation system used to solve the localization task are also presented in Section II. The receiver architecture, the receiver electronics, the measurement setup and the receiver arrangement are presented in Section III. In Section IV the results of preliminary localization measurements are shown. We also performed simulations to analyze the improvement in the localization accuracy by using more than two receivers. The simulation method and the simulation results are listed in Section V followed by the conclusion in Section VI.

II. PRELIMINARY WORK

For the sensor data transmission and for solving the localization task the well defined properties of magnetic fields are used.

A. Data Transmission

The propagation characteristics of magnetic fields do not differ between water and air due to their similar magnetic permeabilities [6]. The radio frequency data transmission, on the other hand suffers from high attenuations in underwater environments [7]. Common used methods for underwater data exchange systems are also the acoustic and the optical data transmission [8]–[10]. We choose the magneto-inductive data transmission since the acoustic and the optical methods are not well suited for our aim. The optical method would not be feasible due to the many obstacles in the reactor; for example the WLEs or the algae. The acoustic method is unsuitable due to the physical separation between transmitter and receiver by the reactor wall. As modulation technique, in order to overlap a digital signal on a carrier wave, we use the on-off keying. This is implemented by switching a hartley-oscillator on and off. The sensor data stream is currently simulated with a bit-generator. The bit-generator is a square wave generator

based on the integrated circuit LM555. The high level of the generated square wave represents the 1-bit and the low level the 0-bit. This signal is used as control signal to switch the hartley-oscillator on and off.

B. Inductive Localization

The magnetic field of a coil with N turns modelled as a dipole field can be described by its radial (H_r) and tangential (H_t) components like shown in (1) and (2), where A is the cross section area of the coil, $I = i \cos(\omega t)$ the exciting current, ρ is the radial distance from the coil centre and ζ the off axis angle [11].

$$H_r = \frac{NIA}{2\pi\rho^3} \cos \zeta \quad (1)$$

$$H_t = \frac{NIA}{4\pi\rho^3} \sin \zeta \quad (2)$$

Equation (3) is the coupling equation between a transmitter and a receiver where both of them have the same orientation ($\vec{e}_{x-rx} = \vec{e}_{x-tx}$ and $\vec{e}_{y-rx} \parallel \vec{e}_{y-tx}$ and $\vec{e}_{z-rx} \parallel \vec{e}_{z-tx}$) [11].

$$\vec{f}_{rx} = \left(\frac{C}{\rho^3}\right) \mathbf{S} \vec{f}_{tx} \quad (3)$$

$$\mathbf{S} = \text{diag}(1 \quad 0.5 \quad 0.5) \quad (4)$$

In (3), the transmitter signal vector is referred to as \vec{f}_{tx} and the receiver signal vector as \vec{f}_{rx} . ρ is the distance between them and C is a constant factor derived from the receiver parameters (coil properties, signal gain). To simplify the localization task, the transmitter coil is assumed to be always aligned with a global z-coordinate like shown in Figure 1. By measuring the x-, y- and z-components of the magnetic field at one position it's possible to calculate a direction vector \vec{r} defined by the angles α and β (see Figure 1) that points from the measuring point to the transmitter position. By measuring the x, y and z magnetic field components at two or more defined positions the localization of the transmitter coil can be calculated by finding the point where the direction vectors of all measuring points comes closest to each other (ideally the intersection). Expanding (3) with the rotation matrix around the z-axis (\mathbf{T}_α)

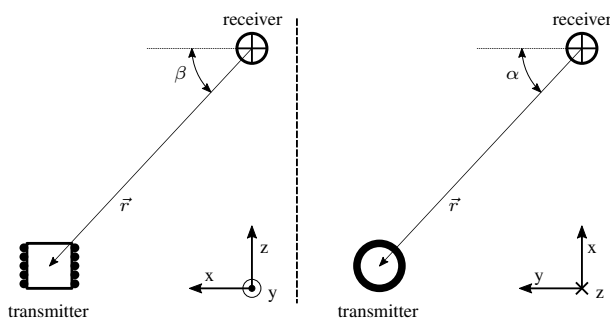


Figure 1. Transmitter-receiver alignment

and the rotation matrix around the y-axis (\mathbf{T}_β), we get (5), which describes the coupling between the transmitter and a receiver in our setup. Solving (5) for the angles α and β enables us to calculate the direction vector \vec{r} . Since we do only transmit in z-direction the transmitter signal vector $\vec{f}_{tx} = [0 \ 0 \ a]^T$ is an unknown value a in z-direction. The

value is assumed as unknown since the transmitting power depends on the actual position of the transmitting coil in the photobioreactor. \vec{f}_{rx} contains the measured field components in x- y- and z-direction.

$$\vec{f}_{rx} = \left(\frac{C}{\rho^3}\right) \mathbf{T}_\alpha^{-1} \mathbf{T}_\beta^{-1} \mathbf{S} \mathbf{T}_\beta \mathbf{T}_\alpha \vec{f}_{tx} \quad (5)$$

We calculate the vector \vec{r} (as an unit vector) from the ratios of the components of the receiver signal vector \vec{f}_{rx} , for that reason the constant factor C/ρ^3 in (5) is omitted.

III. EXPERIMENTAL SETUP

In order to solve the localization task described by (5) in Section II, the receivers need the ability to measure the magnetic field in all three spatial directions at a defined position. This section discusses the design and the arrangement of the receivers as well as the measurement setup used to perform preliminary localization measurements.

A. Design of the receiver

We developed a receiver design with three coils where each of them are placed orthogonally to the other two (like shown in Figure 2) in order to measure the x-, y-, and z-components of the transmitter magnetic field at one point. The first version of the receiver electronic circuit was based on a LC-Tank tuned to the transmitter frequency. Therefore, each receiver coil was connected in parallel with a capacitor and a resistance. In

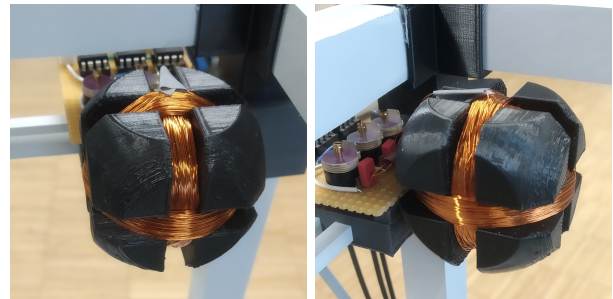


Figure 2. Receiver coils

contrast to the theory, the mutual inductances between the orthogonally placed coils are not zero in practice. The use of LC-Tanks as a main receiver architecture was therefore dismissed since they lead to mutual oscillations of the three oscillators because of the existing minimal mutual inductions. So, we choose to use an active resonant filter tuned to the transmitter frequency in order to amplify the signal which is inducted in each receiver coil. Figure 3 shows its circuit where the receiver coil would be connected to the pin V_{in} . The filter amplifies the signal at the resonant frequency by the gain factor of $|G| \approx 200$ as can be seen from its frequency response in Figure 4. In order to enable a manual calibration of the resonant frequency, the capacitor C_1 (see Figure 3) has been realized as a parallel connection of a variable capacitor and a fixed one. The resistance R_1 has been realized as a potentiometer to enable an adjustment of the gain factor.

B. Arrangement of the receivers

By calculating the angles α and β with (5), we get multiple possible solutions for the direction vector \vec{r} per receiver. The

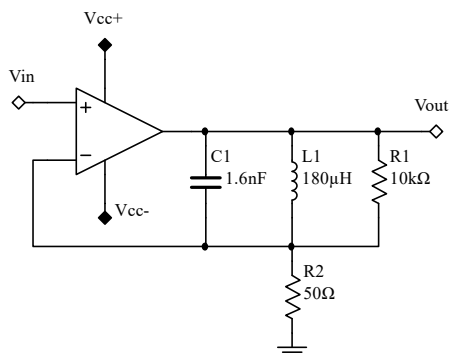


Figure 3. Active resonant filter

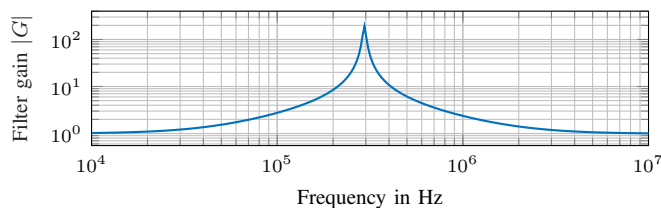


Figure 4. Frequency response of the active resonant filter

reason for that is the rotation symmetry of the magnetic field of a round coil. Positioning the receivers at crucial positions, the possible solutions can be diminished to one useful solution for each receiver. If the receiver is placed at a corner of the region of interest, the number of possible solutions for the direction vector is automatically diminished to one. Figure 5 shows the arrangement used for the first localization measurements. The

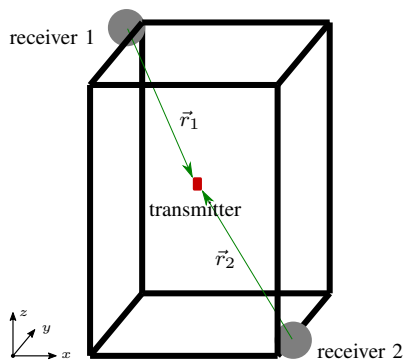


Figure 5. Receiver arrangement

receiver signals were digitalized with the *National Instruments USB6366* I/O device. The software *Matlab* by *MathWorks* is used to control the I/O device and for solving (5) in order to calculate the transmitter position.

IV. MEASUREMENT RESULTS

We performed localization measurements with a two receiver setup like shown in Figure 5. The height (z) and width (x) of our setup construction is 50 cm, the depth (y) is 30 cm. The setup is entirely made out of plastic materials in order to not influence the magnetic field. We performed measurements with the same x - and y -positions at different heights. The measured positions are compared to the exact ones in Figure 6

for a constant height of $z = 25$ cm. The maximum absolute errors per coordinate for the measurements shown in Figure 6 are:

- max abs. error x -coordinate = 3.9 cm
- max abs. error y -coordinate = 2.4 cm
- max abs. error z -coordinate = 4.7 cm

Figure 7 shows the mean values of all relative errors (x -, y -, and z -coordinates) referred to the test setup dimensions for different heights (the five x - and y -coordinates are the same at each height).

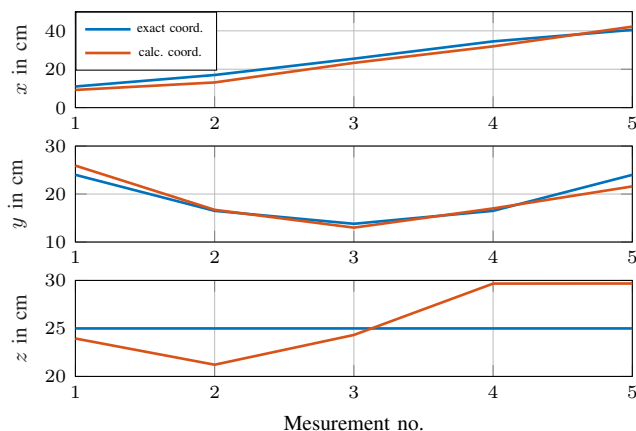


Figure 6. Exakt coordinates vs. measured coordinates

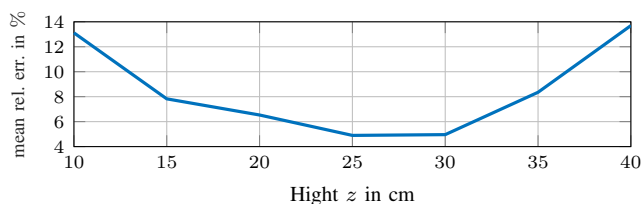


Figure 7. Mean values of the relative errors of all three coordinates at different heights

V. SIMULATION: ACCURACY IMPROVEMENT BY USING THREE OR MORE RECEIVERS

We performed preliminary simulations where the differences in accuracy were calculated between a two receiver setup and a setup with three or more receivers in order to get an idea about the improvement of the overall accuracy. We use *Matlab* by *MathWorks* to calculate the signal amplitudes in x -, y -, and z -direction for each receiver, for a given transmitter position. With the calculated amplitudes sinus signals were generated and three types of noise/signal interferences were added:

- variation of the signal amplitude
- overlap of the power supply magnetic field signal
- overlap of white noise

For the simulations no. 1 and 2 in Table I, the signal amplitude is varied using random values in the range between 0 and 5% of the calculated exact amplitude. White noise is added using random values in the range between 0 and 50% of the signal amplitude and the power supply signal is added with the same amplitude as the calculated clean receiver

signal amplitude. For the simulations no. 3 and 4, the signal amplitude is varied randomly in the range between 0 and 15%. The other parameters were left as for measurements no. 1 and 2. With these constrains the difference vector \vec{d} between the calculated position and the exact position is determined for over 7000 transmitter positions in our region of interest shown in Figure 5. The third receiver is placed in the upper right corner over the receiver 2. The fourth receiver is placed in the lower front left corner and the fifth receiver in the upper back right corner of our region of interest. As a measure of accuracy we use the length of the difference vectors between the exact and the calculated positions. In Table I the mean values of the difference vector lengths of all measurements are listed for setups with two to five receivers. It can be seen that the length of the difference vectors decreases by more than half if the setup with two receivers is compared to the setup with three receivers. By using more than three receivers the improvement gets smaller.

TABLE I. MEAN VALUES IN CM OF THE DIFFERENCE VECTORS FOR THE TWO RECEIVER SETUP AND THE THREE RECEIVER SETUP

sim. no.	sig. ampli. variation	calc. pos.	mean $ \vec{d} $ 2 rec.	mean $ \vec{d} $ 3 rec.	mean $ \vec{d} $ 4 rec.	mean $ \vec{d} $ 5 rec.
1	max. 5%	7057	3.52 cm	1.55 cm	1.31 cm	1.02 cm
2	max. 5%	7057	3.51 cm	1.55 cm	1.29 cm	1.01 cm
3	max. 15%	7057	10.53 cm	4.62 cm	3.83 cm	3.09 cm
4	max. 15%	7057	10.38 cm	4.50 cm	3.89 cm	3.07 cm

VI. CONCLUSION

For the measurements described in Section IV, the major deviations from the exact position can be found in the z-coordinate. It can be seen from Figure 7 that the overall highest accuracy is reached at approx. half the height (z-coordinate) between receiver 1 and receiver 2. For low z-coordinates or for high z-coordinates the distance to one receiver gets bigger and the accuracy gets lower.

The feasibility of the method has been shown. The future aim is to improve the overall accuracy. We already showed in Section V that the inaccuracy can diminished by more then a half by using a third receiver.

The position of the transmitter is now calculated by evaluating the ratios of the components of the receiver signal vector \vec{f}_{rx} individually for each receiver. In future, in order to improve the accuracy, the sum of the amplitudes will be compared between the receivers, this should yield additional information about the sensor position. The orientation of the receiver plays an important role on the overall accuracy of this system. For the case that the receiver is not aligned with the overall coordinate system, the coupling equation between the transmitter and the receiver has to be adopted by adding some more rotation matrices for the three receiver orientation angles. In future work our approach will be to calculate an optimization for the receiver orientation and position in order to minimize the susceptibility to overall inaccuracies. Imperfections in the orientation of the transmitter also leads to measurement inaccuracies. To counteract this problem, a solution could be the search for a minimum in the coupling equation expanded by the rotation matrices for a transmitter inclination using the position coordinates calculated with the (5) as initial values.

REFERENCES

- [1] M. Heining, A. Sutor, S. Stute, C. Lindnerberger, and R. Buchholz, "Internal illumination of photobioreactors via wireless light emitters: a proof of concept," *Journal of Applied Phycology*, vol. 27, 2015, pp. 59–66.
- [2] A. Sutor, M. Heining, and R. Buchholz, "A class-e amplifier for a loosely coupled inductive power transfer system with multiple receivers," *Energies*, vol. 12, no. 6, 2019.
- [3] B. O. Burek, A. Sutor, D. W. Bahnemann, and J. Z. Bloh, "Completely integrated wirelessly-powered photocatalyst-coated spheres as a novel means to perform heterogeneous photocatalytic reactions," *Catal. Sci. Technol.*, vol. 7, no. 21, 2017, pp. 4977–4983.
- [4] T. Lauterbach et al., "Sens-o-spheres – mobile, miniaturisierte sensorplattform für die ortsungebundene prozessmessung in reaktionsgefäßen," 13. Dresdner Sensor-Symposium 2017, Hotel Elbflorenz, Dresden, 12 2017, pp. 89 – 93.
- [5] D. Demetz, O. Zott, and A. Sutor, "Wireless and traceable sensors for internally illuminated photoreactors," in 2020 IEEE International Conference on Industrial Technology (ICIT), 2020, pp. 582–586.
- [6] M. C. Domingo, "Magnetic induction for underwater wireless communication networks," *IEEE Transactions on Antennas and Propagation*, vol. 60, no. 6, June 2012, pp. 2929–2939.
- [7] U. M. Qureshi et al., "Rf path and absorption loss estimation for underwater wireless sensor networks in different water environments," *Sensors*, vol. 16, no. 6, 2016.
- [8] X. Che, I. Wells, G. Dickers, P. Kear, and X. Gong, "Re-evaluation of rf electromagnetic communication in underwater sensor networks," *IEEE Communications Magazine*, vol. 48, no. 12, December 2010, pp. 143–151.
- [9] Y. Li, H. Yin, X. Ji, and B. Wu, "Design and implementation of underwater wireless optical communication system with high-speed and full-duplex using blue/green light," in 2018 10th International Conference on Communication Software and Networks (ICCSN), July 2018, pp. 99–103.
- [10] J. Shi, S. Zhang, and C. Yang, "High frequency rf based non-contact underwater communication," in 2012 Oceans - Yeosu, May 2012, pp. 1–6.
- [11] F. H. Raab, E. B. Blood, T. O. Steiner, and H. R. Jones, "Magnetic position and orientation tracking system," *IEEE Transactions on Aerospace and Electronic Systems*, vol. AES-15, no. 5, Sep. 1979, pp. 709–718.

Towards Joint Cell Selection and Task Offloading in Cellular IoT Systems with Edge Computing

Edgar Adrian Esquivel-Mendiola, Sergio Pérez-Picazo, Hiram Galeana-Zapién

Centro de Investigación y de Estudios Avanzados del I.P.N. (Cinvestav)
Cinvestav Tamaulipas
Ciudad Victoria, México
email: {edgar.esquivel,sergio.perez.picazo,hiram.galeana}@cinvestav.mx

Abstract—Mobile Edge Computing (MEC) in cellular networks aims to bring computational capabilities close to end-users to reduce the latency of applications on the Internet of Things (IoT). This is particularly crucial to computation-intensive IoT broadband applications (e.g., video analytics, augmented reality, etc.) demanding a data processing task to be performed within a given time threshold. In this regard, the task offloading problem has been investigated in the literature in order to achieve an appropriate trade-off between energy and latency. However, there is a need for the joint design of task offloading mechanisms and cell selection algorithm as a mean to select the most appropriate to each device in order to meet delay requirements and fulfill resource constraints at the MEC server site. In this paper, we present the foreseen framework to tackle such a challenging problem.

Keywords—Delay-sensitive applications, internet of things, mobile edge computing, offloading.

I. INTRODUCTION

The Internet of Things (IoT) is the most recent evolution of the Internet technologies and services. In this novel paradigm, everyday objects will be equipped with communication, computing and sensing capabilities to collect data from their environment. The analysis of the collected data is expected to enable knowledge-based decisions and to produce value-added services in domains like healthcare, manufacturing, logistics, etc. Broadly speaking, IoT applications in such domains could be categorized according to the communication requirements (i.e., data throughput, data volume, latency, etc.), or in terms of the IoT device capabilities (low-cost fixed/mobile sensor, smartphone, wearable, etc.). In this context, the fifth generation (5G) mobile communication system will play a key role in the IoT ecosystem by providing wireless connectivity to IoT *mobile* devices dispersed over large areas and demanding stringent Quality of Service (QoS) levels. For instance, the 5G network is expected to support a major IoT market segment related to next-generation broadband and critical services having low delay requirements and heavy computational-resource needs. Towards providing flexible support of these IoT applications' categories, enabling cellular technologies, such as 5G new radio (NR), Long-Term Evolution (LTE) for Machine Type Communication (MTC), a.k.a. LTE-M, and Narrowband IoT (NB-IoT) have been proposed. Additionally, in order to reduce service latencies, the Mobile Edge Computing (MEC) aims to bring storage and computational resources close to end devices in the Radio Access Network (RAN) [1]. This implies the

deployment of MEC servers co-located in the cell site with the Base Station (BS). This allows reducing the round-trip latency for applications that offload data from terminals to the network for data processing purposes and wait for the outcomes. Such a data processing is preferred to be performed at the network edge in order to avoid sending big amounts of traffic from the network edge through the backhaul towards more distant central computing resources (i.e., mobile cloud computing paradigm). In this sense, one of the main challenges is that MEC servers are generally known to be constrained by the amount of computation resources, implying that they might be easily overloaded due to intensive computation requests from IoT broadband applications. Another important resource constraint in the RAN is the available radio resources.

Under such a distributed computing environment, the task offloading problem has been subject of study in the literature aiming to determine if a given task is computed locally (at the mobile device) or at the network edge. However, as intensive computation tasks are energy-consuming, on-device computation approaches severely affect the lifetime of battery-limited devices. In order to address these challenges, different computation task models for full or partial data offloading have been explored in the literature [2], where some degrees of freedom could be allowed by considering soft deadline requirements (i.e., portions of data to be computed after a time threshold). The task offloading problem aims to achieve a trade-off between energy efficiency at mobile devices and end-to-end delay of applications. This latter aspect involves the appropriate modeling of delay components for data processing (at the mobile device or network edge node) and data transmission over wireless channel. At this regard, the task offloading problem it is commonly analyzed under the assumption that each mobile device is already assigned to a MEC server according to a cell selection criterion aimed to optimize radio link efficiency (e.g., minimum path loss, max-SINR, etc.). Nevertheless, such cell selection approaches neglect other aspects that could greatly influence the obtained Quality of Service (QoS), such as selecting an overloaded MEC server or a BS with exhausted radio resources.

In this paper, we describe our work in progress where the aim is to develop an integral framework to jointly optimize the offloading decisions and the cell selection. Specifically, we formulate an optimization problem aimed to determine the most appropriate serving cell to each device attending

to: a) radio channel bandwidth in the cell, and b) computing capacity of the MEC server, and c) energy constraints of mobile devices. We aim to determine the cell selection solution that provides the minimum the system performance delay in MEC-based IoT scenarios. Such a framework involves a number of challenges. First, the algorithms to be developed should work in distributed computing environments, implying that each edge node should perform resource allocation decisions independently based on local information. To this end, distributed iterative algorithms based on a pricing-based scheme (where the assignment process behaves as a bidding process that iteratively allocate edge resources to end users) are considered as a potential algorithmic solution. Second, realizing low-latency and energy-efficient in MEC scenarios demand joint radio and computational management schemes. It is well known that wireless channel conditions (path loss, interference, etc.) affects the amount of energy consumption required for data offloading. That is, poor channel conditions are likely to lead to low achievable data rate at the air interface, implying and increased energy consumption at the mobile device as well as transmission latency.

Attending to the aforementioned arguments, this paper presents a work in progress that aims at investigating integrated task offloading and cell selection approaches able to, for instance, select a given cell with favorable channel conditions to perform data offloading. The rest of the paper is organized as follows. Section II presents the related work. Section III presents the foreseen technical approach. Section IV details the envisioned contributions and also concludes the paper.

II. STATE OF THE ART

The task offloading problem has been studied in the literature with the aim of determine the appropriated site to perform the task processing according to the conditions observed in the system (i.e., energy constraints, latency requirements, channel conditions, computing capabilities). Some of the proposed solutions are based on greedy solutions, heuristics and well-known approaches from the literature. Several research works have tackled the task offloading problem in MEC-like system deployments. The most relevant approaches proposed so far are summarized in Table I, focusing on key aspects such as energy and latency requirements, type of task offloading (full or partial), algorithm type. We also highlight that the vast majority of existing approaches does not include the cell selection problem (i.e., tasks offloading is tackled assumed for a given cell selection solution). In what follows, we provide a brief analysis of the related work.

Huang *et al.* [3] proposed an algorithm to dynamically perform the task offloading process taking into account the wireless status. This approach is based on the Lyapunov optimization algorithm, which aims to improve the energy consumption [4], while satisfies the execution time required for mobile application. However, the authors do not consider the support of IoT devices in the cellular system. Similarly, Zhang *et al.* [5] proposed a mechanism to minimize the energy consumption during task offloading with MEC, although this work provides a support of multiple devices under a 5G heterogeneous network, it does not consider the main IoT scenarios for task offloading and assume that the MEC servers are not constrained. The results demonstrated that energy consumption can differ with the number of mobile devices, so there is

not a lineal relation between them. Yu *et al.* [6] proposed an algorithm for task offloading dynamically. The main objective of this approach is to minimize the cost generated by the network through the development of supervised deep learning model. In contrast to other proposals, this implementation is modeled as a classification problem to search an alternative for task offloading process considering the network conditions. Similarly, Chen *et al.* [7] proposed an adaptative algorithm for task offloading at the same time it considers the capabilities MEC paradigm offer. The algorithm dynamically decide when to perform the task offloading process based on the network status. According to the authors, this work was evaluated with two real world applications: license plates recognition and voice recognition. As a result, the algorithm reduces the energy consumption without considering the capacity restrictions of the MEC server.

As shown in Table I, a drawback of existing approaches is that are proposed for centralized solutions where based on the complete information of the system determines the offloading of the tasks. Furthermore, most of the studied works do not consider the joint cell selection and delay minimization problem, instead they assume a previous assignment, which is mainly based on greedy solutions. In this sense, our envisioned solution described in the next section aims to design a joint cell selection and delay minimization algorithm, which operating in a distributed way at each BS determines the appropriated BS to offload the task according to delay and energy constraints.

III. FORESEEN RESEARCH WORK

This research aims to investigate novel joint cell selection and task offloading solutions to provide enhanced support of delay-sensitive services demanding computation-intensive capabilities. This section presents the foreseen technical approach towards this challenging problem. Namely, we present the system model and the corresponding optimization problem that we are targeting.

A. System Model

The system model is illustrated in Figure 1. We consider a cellular deployment with N cell sites and M IoT devices in the service area. In each cell site, a MEC server is assumed to be co-located with the BS equipment. Accordingly, the following resource constraints per site are considered: a) radio channel bandwidth used in the BS, and b) computing capacity of the MEC server. In addition, in line with LTE/4G and NR/5G radio interfaces, we assume OFDMA as an access method in the air interface so that the total system bandwidth W is divided into K resource blocks according to a frequency reuse pattern. Therefore, the amount of radio resources is defined in terms of the K_j resource blocks assigned to each BS $j \in N$. Finally, it is worth clarifying that backhaul resources are not considered in the present modelling as all tasks are assumed to be processed either at the mobile device or the network edge. In other words, in collaborative approaches between edge and cloud computing resources, the described system model could be easily extended by assuming that each cell site is connected to the network core and central clouds by means of a backhaul network with finite link bandwidth at each BS.

Additionally, we assume that each IoT device i have specific delay and computation requirements to process task A_i , which cannot be partitioned and should be processed as

TABLE I. SUMMARY OF RELATED WORK.

Author	Year	Cell Selection	Algorithm	Task Offloading Type	Saved Energy	Reduce Latency
Xiang <i>et al.</i> [8]	2019	No	Fragment algorithm for data processing	Full	No	Yes
Ning <i>et al.</i> [9]	2019	No	Hybrid offloading algorithm	Full	No	No
Sun <i>et al.</i> [10]	2019	No	Hybrid offloading algorithm	Partial	No	Yes
Chen <i>et al.</i> [7]	2019	No	Adaptative offloading algorithm	Full	Yes	Yes
Sun <i>et al.</i> [11]	2018	No	Greedy algorithm	Full	Yes	Yes
Wu <i>et al.</i> [12]	2018	No	Offloading algorithm based on environment identification	Partial	Yes	No
Yu <i>et al.</i> [6]	2017	No	Heuristic	Partial	Yes	No
Deng <i>et al.</i> [13]	2016	No	Adaptative offloading algorithm for multiple users	Full	No	No
Zhang <i>et al.</i> [5]	2016	No	Efficient computing algorithm	Partial	Yes	No
Huang <i>et al.</i> [3]	2012	No	Dynamic data offloading algorithm in IoT devices	Partial	Yes	Yes

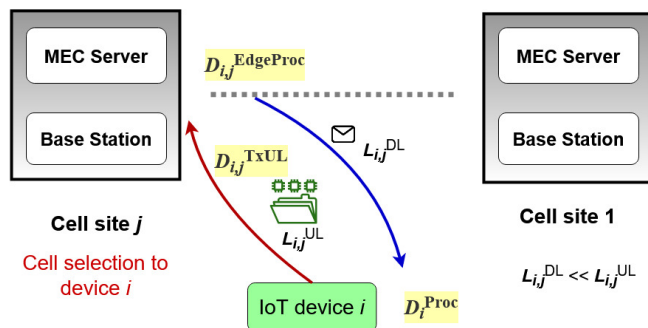


Figure 1. System Model.

a whole either at the mobile device or edge node collocated with the cell j serving the device (e.g., video stream analysis [2]). Each computation task is modeled using a three-field notation $A_i(L_{i,j}^{UL}, \gamma_{i,j}, D_i^{\text{req}})$, where $L_{i,j}^{UL}$ is the input data file (in bits) to be transferred through the uplink wireless channel to the selected edge node j , $\gamma_{i,j}$ denotes the workload (CPU cycles/bit) for processing one-bit data, and D_i^{req} is the hard deadline imposed by the application to further process the file and receive the corresponding response. In this sense, as illustrated in Figure 1, the total delay experienced by a file from a given device can be expressed as:

$$D_{ij} = \varphi_i D_i^{\text{proc}} + [(1 - \varphi_i)(D_{i,j}^{\text{TxUL}} + D_{i,j}^{\text{EdgeProc}} + D_{i,j}^{\text{TxDL}})] \quad (1)$$

where $\varphi_i \in \{0, 1\}$ is a variable that is equal to 1 if the task is processed locally at the device i , or 0 if it is offloaded to the mobile edge for processing purposes. Moreover, the terms $D_{i,j}^{\text{TxUL}}$ and $D_{i,j}^{\text{TxDL}}$ denote the transmission delays in the uplink and downlink, respectively, which can be derived based on the corresponding transmission rates and the length of the data to be offloaded. Notice that $L_{i,j}^{\text{DL}} \ll L_{i,j}^{\text{UL}}$ could be assumed due that the response from the edge server to the mobile device is smaller in size than the data offloaded to

the MEC server. Furthermore, D_i^{proc} and $D_{i,j}^{\text{EdgeProc}}$ are the delay observed if the task is processed at the mobile device or MEC server, respectively. Following the formulation presented in [14], we define the processing delay D_i^{proc} and $D_{i,j}^{\text{EdgeProc}}$ as follows:

$$D_i^{\text{proc}} = \frac{L_{i,j}^{UL} \gamma_{i,j}}{C_i^{\text{Device}}} \quad (2)$$

where C_i^{Device} denotes the computing capacity (CPU cycles/sec) of the mobile device. Similarly, the processing delay at the MEC server can be computed as follows:

$$D_{ij}^{\text{EdgeProc}} = \frac{L_{i,j}^{UL} \gamma_{i,j}}{C_{i,j}^{\text{Edge}}} \quad (3)$$

where $C_{i,j}^{\text{Edge}}$ denotes the amount of computing resources (CPU cycles/sec.) assigned by the edge node j to process the task of device i . Furthermore, we can estimate the energy consumption for the task processing at the mobile device as follows [15]:

$$E_i = (L_i^{\text{UL}} \gamma_i) f_i \quad (4)$$

where f_i denotes the required energy to process one bit at the mobile device. The residual energy could provide an appropriate hint to decide if a task is offloaded or computed locally. In addition, Equation (4) could be extended to include the energy consumption required to transmit the task to the BS node.

B. Problem Formulation

Let $b_{i,j} = 1$ the variable denoting whether or not device i is associated with BS computing node j to offload tasks. The joint cell selection and task offloading is that of determining the most appropriate assignment $B = \{b_{i,j}\}$ in order to minimize total delay of all devices while satisfying the computing resources at each node j as well as the energy constraint of IoT devices. The problem formulation can be written as follows:

$$\min \sum_{j=1}^N \sum_{i=1}^M D_{ij} b_{i,j} \quad (5)$$

$$\text{s.t.} \quad \sum_{i=1}^M C_{i,j}^{\text{Edge}} b_{i,j} \leq 1, \quad j = 1, \dots, N \quad (6)$$

$$D_{ij} \leq D_i^{\text{req}}, \quad i = 1, \dots, M \quad (7)$$

$$\sum_{j=1}^N b_{i,j} \leq 1, \quad i = 1, \dots, M \quad (8)$$

$$b_{i,j} \in \{0, 1\} \quad (9)$$

where (5) is the objective function defined in terms of delay experienced by the application. In the case of constraint (6), for each connected user node j will allocate an amount of computing resources denoted as $C_{i,j}^{\text{Edge}}$, so the allocation of a total of devices to an edge node should not exceed the maximum available computing capacity. In the constraint (7), the delay $D_{i,j}$ refers to the sum of various delay components considering the processing time (in MEC node j or locally on device i) and transmission time on the wireless interface. In either case, the total delay must satisfy the latency requirement of the application.

The problem (5)-(9) is a combinatorial optimization problem due to the binary variable $b_{i,j}$, so that solving the problem with exact algorithms may be difficult even for a small number of N and M . We aim to refine such a problem in order to make it more tractable, e.g., reducing the number of constraints and to model the association process as a message passing based on pricing values of BSs. In that way, dual decomposition theory could be applied to design a distributed approach to solve the above problem. More specifically, the above formulated problem could be refined depending on the implementation and validation of the envisioned algorithms. In order to narrow down the joint cell selection and task offloading problem, we consider the following Research Questions (RQ):

- **RQ1:** ι Is it possible to design a cell selection criteria to steer device associations based on radio/computation conditions at the MEC servers and delay requirements of applications?
- **RQ2:** ι How to design an efficient distributed cell selection algorithm that operating with network partial state information could find the optimal assignment of communication and computation resources in order to minimize the system delay?
- **RQ3:** ι How to properly model a decision making mechanism to determine if a task should be processed locally, at the MEC server or a partial offloading?

We aim to conduct Montecarlo simulations to evaluate the performance of our joint cell selection and task offloading approach. Moreover, two task offloading approaches from the literature will be used for benchmarking purposes. The evaluation will be carried out in terms of the total average delay achieved by the algorithms when offloading the tasks to the edge server or computed locally at the mobile device. On the one hand, we are interested in analyzing the suitability of assigning mobile device i to edge server j in order to meet

the delay requirement imposed by task A_i . In this sense, we aim to demonstrate that a cell selection procedure that accounts for computing capacity of edge servers and delay requirements from mobile devices, lead to better performance in terms of overall system delay. Hence, a set of simulations varying the available system bandwidth and the delay requirements from applications are considered in the experimental analysis. On the other hand, we want to evaluate the computing delay conditions associated to the task processing under the variation of the availability of computing capabilities at the devices and the MEC servers. At this regard, we aim to compare the proposed solution with related works from the literature that are based on both computing and joint computing-communication constraints.

IV. CONCLUSION AND FUTURE WORKS

In order to complement the design of task offloading schemes in MEC scenarios, we studied the integration of wireless channel conditions into a joint formulation. In particular, we have described the design of a joint task offloading and cell selection schemes able to determine the serving cell (MEC server) to each mobile device taking into account device and network resource constraints and QoS requirements of applications. We have discussed that the design of task offloading solutions it is commonly tackled from a mobile computing perspective (i.e., reduce energy consumption, etc.), whereas few attention has been paid on how the cell selection procedure would severely impact the observed latency due to, for instance, the assignment of a device to an overloaded cell. Taking this into account, we presented a work in progress towards a novel task offloading and cell selection framework to drive the assignment decisions based on applications' requirements and the availability of radio and computing resources at the MEC servers. Finally, we described the experimental simulation to be used for validating our proposed approach.

REFERENCES

- [1] N. Hassan, S. Gillani, E. Ahmed, I. Yaqoob, and M. Imran, "The role of edge computing in internet of things," IEEE Communications Magazine, August 2018, pp. 1–6.
- [2] Y. Mao, C. You, J. Zhang, K. Huang, and K. B. Letaief, "A survey on mobile edge computing: The communication perspective," IEEE Communications Surveys Tutorials, vol. 19, no. 4, 2017, pp. 2322–2358.
- [3] D. Huang, P. Wang, and D. Niyato, "A dynamic offloading algorithm for mobile computing," IEEE Transactions on Wireless Communications, vol. 11, no. 6, 2012, pp. 1991–1995.
- [4] S. Ou, K. Yang, and J. Zhang, "An effective offloading middleware for pervasive services on mobile devices," Pervasive and Mobile Computing, vol. 3, no. 4, 2007, pp. 362–385.
- [5] K. Zhang et al., "Energy-efficient offloading for mobile edge computing in 5g heterogeneous networks," IEEE access, vol. 4, 2016, pp. 5896–5907.
- [6] S. Yu, X. Wang, and R. Langar, "Computation offloading for mobile edge computing: A deep learning approach," in 2017 IEEE 28th Annual International Symposium on Personal, Indoor, and Mobile Radio Communications (PIMRC). IEEE, 2017, pp. 1–6.
- [7] X. Chen et al., "An adaptive offloading framework for android applications in mobile edge computing," Science China Information Sciences, vol. 62, no. 8, 2019, p. 82102.
- [8] B. Xiang, J. Elias, F. Martignon, and E. Di Nitto, "Joint network slicing and mobile edge computing in 5g networks," in ICC 2019-2019 IEEE International Conference on Communications (ICC). IEEE, 2019, pp. 1–7.

- [9] Z. Ning, X. Wang, J. J. Rodrigues, and F. Xia, "Joint computation offloading, power allocation, and channel assignment for 5g-enabled traffic management systems," *IEEE Transactions on Industrial Informatics*, vol. 15, no. 5, 2019, pp. 3058–3067.
- [10] H. Sun, F. Zhou, and R. Q. Hu, "Joint offloading and computation energy efficiency maximization in a mobile edge computing system," *IEEE Transactions on Vehicular Technology*, vol. 68, no. 3, 2019, pp. 3052–3056.
- [11] Y. Sun, Z. Hao, and Y. Zhang, "An efficient offloading scheme for mec system considering delay and energy consumption," *Journal of Physics: Conference Series*, vol. 960, 01 2018, p. 012002.
- [12] H. Wu, Y. Sun, and K. Wolter, "Energy-efficient decision making for mobile cloud offloading," *IEEE Transactions on Cloud Computing*, vol. 8, no. 2, 2020, pp. 570–584.
- [13] M. Deng, H. Tian, and X. Lyu, "Adaptive sequential offloading game for multi-cell mobile edge computing," in *2016 23rd international conference on telecommunications (ICT)*. IEEE, 2016, pp. 1–5.
- [14] W. Almughalles, R. Chai, J. Lin, and A. Zubair, "Task execution latency minimization-based joint computation offloading and cell selection for mec-enabled hetnets," in *2019 28th Wireless and Optical Communications Conference (WOCC)*, 2019, pp. 1–5.
- [15] Y. Pei, Z. Peng, W. Zhenling, and H. Wang, "Energy-efficient mobile edge computing: Three-tier computing under heterogeneous networks," *Wireless Communications and Mobile Computing*, vol. 2020, 04 2020, pp. 1–17.

Rapid Detection of Toxic Emissions Using DNN Based Sensing

Ibrahim Bhavnagarwala

Danbury High School

Danbury CT USA

e-mail: ibha1056@danbury.k12.ct.us

Adam Bhavnagarwala

Danbury High School

Danbury CT USA

e-mail: abha1055@danbury.k12.ct.us

Abstract— Smoking remains one of the top 3 causes of illness in the US; it is one of top 5 causes of fire hazards in a home and is the single most preventable cause of illness and premature death in the US. The use of Deep Neural Networks (DNN) is demonstrated to detect cigarette smoke much sooner and with much higher accuracy than conventional smoke/carbon monoxide detectors used today. The hardware demonstration and prototype engages machine learning to not only discriminate cigarettes from other sources of smoke and carbon monoxide such as burning coal, wood or food – typically not possible with conventional smoke detectors, but also to accurately detect cigarette smoke produced in a room from a single cigarette when concentrations of component gases of cigarette smoke are extremely low. Our prototype also demonstrates the opportunity to classify and discriminate different levels of toxicity and flammability for spaces used by different people.

Keywords- DNN; IoT; Cigarette; Toxic; Detection; Sensors

I. INTRODUCTION

Secondhand smoke is a serious health hazard causing more than 41,000 deaths per year [1]. Secondhand smoke is not risk-free and even short-term exposure can potentially increase the risk of heart attacks. Secondhand smoke contains chemicals known to be harmful. These include formaldehyde, benzene, vinyl chloride, arsenic ammonia and hydrogen cyanide [2]. Smoking is not just a health hazard but also a significant fire hazard. The National Fire Protection Association (NFPA) reports [3] During 2012-2016, an estimated annual average of 18,100 (5%) or, one in 20 home (5%) structure fires were started by smoking materials. These fires caused almost one in four (23%) home fire deaths, and one in 10 (10%) home fire injuries.

Conventional smoke detectors are mostly responsive to carbon monoxide and generally trigger an alarm when the concentration of carbon monoxide exceeds a given threshold. These detectors are also generally agnostic to the source of carbon monoxide and cannot discriminate cigarettes from burning coal, wood or food. The urgency to detect cigarette smoke – especially for people vulnerable to secondhand smoke or other toxic gases is much higher and warrants a trigger at a much earlier time. The trigger should also not require the concentration of cigarette smoke in the air to be as high as conventional detectors since early warning can potentially remove the source of cigarette smoke in areas especially sensitive to second hand smoke

such as Hospitals. The detection of cigarette smoke should also be consistently accurate even at low concentrations of the components of cigarette smoke such as hydrogen cyanide, formaldehyde, benzene and carbon monoxide.

The rest of the paper is structured as follows: Sections II & III describe conventional gas detector technology, methods and their weakness. Sections IV and V describe our prototype hardware used with AI algorithms instead and measurements. Section VI discusses the Training accuracy and loss of our DNN algorithms.

II. CONVENTIONAL DETECTOR TECHNOLOGY AND USE

Conventional gas detectors have evolved in their technology and how they are used as the need to detect CO and fires is emphasized by NFPA regulations.

A. Technology

Conventional gas detectors use a metal oxide sensor to measure the concentration of specific gases. Typically employed to prevent toxic exposure and fire, these cover a range of gases in the flammable and toxic range but most detectors include CO sensors. The metal oxide sensor technologies [4] work by engaging the relationship between electrical conductivity and oxygen partial pressure of a metal oxide sensor. The resistance of the sensor correlates to the concentration of the reducing gas. MQ Sensor modules include op-amp comparators and digital output pins to provide an indication of the presence of gases. Where a quantified measure of the amount of gas (in ppm) is needed, the bare sensor is used in conjunction with a microcontroller.

B. Methods and Limitations

The sensors used in Google Nest (2nd gen) [5] include the Smoke Split-spectrum sensor that detects the presence of smoke in the air using two wavelengths of light to look for smoke. An infrared light is used to detect larger particles generated by slow, smoldering fires, while a blue light detects smaller particles created by fast fires. All of commercially available sensors rely on the sensor itself to identify smoke, fires, flammable or toxic gases. Their common weakness is that detection of smoke, fire occurs too late when the premises are already on fire or when the concentrations of toxic/flammable gases are already dangerously high to be able to trigger the sensor. The primary cause for home structure fires – unextinguished and undetected cigarette butts cannot be detected by conventional detectors simply because the concentrations of emissions

produced by a single cigarette are too low to trigger conventional detectors.

III. SENSORS AND METHODS USED

We used industry standard MQ sensors but our methods to detect toxic and flammable gases relied on measurements of changes in patterns of component gas concentrations and their recognition instead of direct measurements of gas concentrations.

A. Pattern Recognition

Pattern recognition works well for toxic gases that have signature patterns of component gases – as typically found in cigarette smoke or vape. Gases found in hospitals (Anesthetic’s, aerosolized medications and chemicals used as a fixative such as formaldehyde, toluene etc.), Waste water treatment plants, Restaurants (CO, CO₂, N₂, CH₄), Mechanical/boiler rooms (refrigerants), Pharmaceutical Labs (HCN), Oil refineries (BTEX), Cold storage (NH₃) and Industrial manufacturing. These classifications help Hospitals, Workplaces and Schools to monitor toxicity and flammability according to the tolerance people have in designated areas to cigarette smoke or other toxic gas emissions

B. Detection Thresholds

Our prototype enables accurate detection of a toxic emission at much lower concentrations of component gases of the emission by using Classifiers trained to detect signature patterns of small changes in these component gas concentrations as measured by MQ sensors using neural networks..

IV. MICROCONTROLLER HARDWARE USED

The easiest way to be able to control and automate the measurement tasks and sequence of data acquisition from an array of sensors is the use of an inexpensive 8b Microcontroller – the primary component of an IoT system.

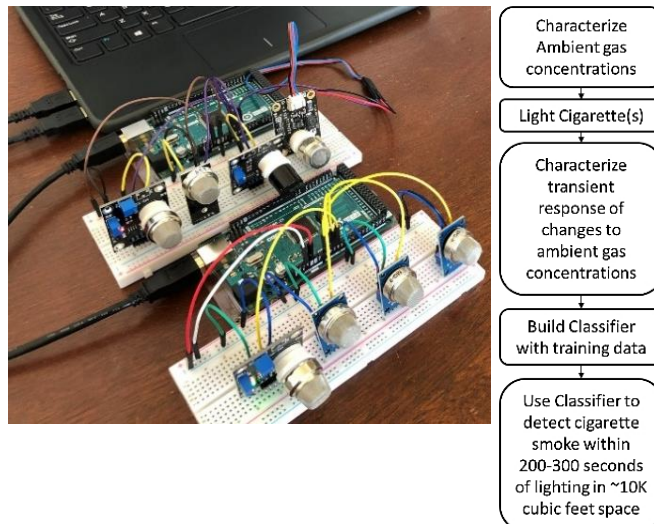


Figure 1. Microcontrollers with an arrays of Gas sensors are used to build a Classifier (top). Measurement flowchart (at right)

A. IoT System Hardware

The IoT type hardware we assembled uses three 8-b RISC Microcontrollers (ATmega2560 in the Arduino mega Dev Board) that can concurrently support 16 sensor IO to collect training data (Figure 1). Conventional sensors used consume significant current (150 mA/sensor at 5V) to heat sensors before they can function. Since the Dev Board sources insufficient current to support all 12 sensors used (Table 1) to capture training datasets, three ‘off-the-shelf’ Dev Boards were engaged to build this prototype. Air was sampled once every 2 seconds by the sensor array to balance size of dataset Vs accuracy delivered. A NodeMCU WiFi module is used to drive sensed data wirelessly for training and/or inference. C-code was developed to read and print the values the sensors sampled every second.

TABLE I: SENSITIVITIES OF AN ARRAY OF GAS SENSORS TO EACH COMPONENT GAS MEASURED BY A SENSOR [7]

Sensor/Gas	MQ2	MQ3	MQ4	MQ5	MQ6	MQ7	MQ8	MQ9	MQ135	MQ136	MQ137	MQ138	MG811
H2	-0.431		-0.275	-0.391	-0.387	-0.936	-0.295				-0.292		
LPG	-0.45	-0.222	-0.379	-0.447	-0.431	-0.122		-0.431					
CH4	-0.324	-0.046	-0.386	-4.278	-0.368	-0.1	-0.085	-0.324				-3.035	
CO	-0.244	-0.162	-0.074	0.13	-0.085	-0.737	-0.06	-0.579	-0.292	-0.292		-	0.2866
CO2									-0.073				-0.104
Alcohol	-0.406	-1.154	-1	-0.205	-0.146	-0.087	-0.06					-0.314	
Propane	-0.528											-0.5	
Benzene		-0.344										-0.301	
Hexane		-0.397											
Smoke			-0.092										
NH3											-0.292		
Toluene													
NH4										-0.431			
H2S										-0.292			
C2H6O											-0.415		
N-Hexane												-0.483	

Data from the sensor array was normalized. By scaling data between 0 and 1, the classifier can read the data more effectively and converge faster [6]

B. Building a Classifier using a DNN

The algorithm used to build this classifier was a Deep Neural Network (DNN). A Deep Neural Network is a certain kind of ML algorithm that is represented as a hierarchical (layered) organization of neurons (similar to the neurons in the brain) with connections to other neurons [6]. Input data is passed through the first layer of the DNN and the hidden layers until it reaches the output layer, which is where the DNN makes a prediction on how to classify the input data [6]. The DNN recognizes patterns in the data and learns how to classify accurately through a learning process which is updating the weights of the neural network through a mechanism called Backpropagation.

The sensor dataset is a quantitative measure of the concentrations of a unique combination of different gases corresponding to a given source (See Table 1). The DNN is used to classify the source of the gases emitted using this data from multiple sensors. The combination of component gases in the corresponding sources measured across several sensors are compiled into ‘training data’ and passed through the DNN. The DNN then learns how to detect the source given the pattern detected by the gas sensor array of the component gas combinations. Prior to the classifier learning the data, the data was split into two parts: the training set and the testing set. The testing set was not used in training and was only used to measure the accuracy of the DNN classifier. The testing set accuracy tells us how well or badly the classifier performed, which gives insight into how to fine-tune the hyperparameters of the DNN.

For the DNN to be able to perform on the data with high accuracy the parameters had to be fine-tuned. After multiple trials the most optimal parameters for the DNN were having 4 layers-14 nodes in the first layer, 13 in the second, 5 in the third, and 1 in the fourth. Also, a dropout chance of 20% was added after every layer before the output. Furthermore, the activation function used for every layer except the output layer was ReLU (Rectified Linear Unit); the activation method for the output layer was a Sigmoid function

C. Measurement Setup

We used a large space (garage) that measures 32' x 20.3' with a 10.5' ceiling. The area and volume of this space is 650 sq ft and 7K ft³. We flushed the air in garage with multiple exhaust fans, and then closed doors giving sensor array enough time to reach a stable unchanging reading as representative of environment (Figure 1). Smoke rises upwards due to it being at a higher temperature when emitted. However, it settles as it cools in the air with sensors placed in our test space a few feet off the ground demonstrating sufficient sensitivity within 300 seconds of lighting the cigarette

V. MEASUREMENTS

Our measurements had a primary goal of characterizing the patterns in component gas concentrations from toxic, flammable and similar but non-toxic emissions such as burning food or incense while also providing enough ‘training’ to the neural network to discriminate gas detection at different levels of toxicity, flammability and also be able to recognize post priori the presence of toxic emissions at a previous time.

A. Speed of Source Detection

We lighted a cigarette and used a bulb syringe to ‘puff’ at the lighted cigarette/vape (neither of us smoke) to emulate emissions typically seen from a cigarette/Vape for 9 minutes. We observed the first response of the sensor to gas emissions from any source was *proportional to the distance the source was from the sensor*. We conclude that the *response time of the sensor is limited by the time it takes for component gases of the source to diffuse through the air to the sensor*. The minimum time it takes for the sensor array to correctly identify the emission source is characterized as the speed of gas detection.

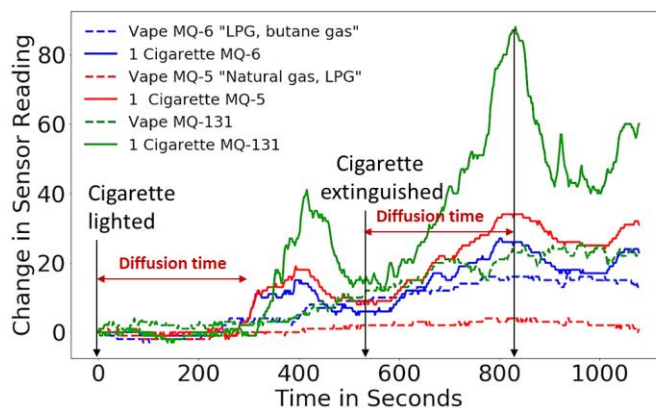


Figure 2. Changes registered in sensor array are different – Cigarette Vs Vape patterns can be discriminated by Classifier (MQ5 responsive to CO as well).

Two peaks were observed at very small changes in concentrations (from a single cigarette/vape) (Fig 2). *The first peak* registers initial contact at sensors of cigarette/vape emissions followed by diffusion away from sensor. *The second peak* registers extinguishing cigarette/vape, diffusion time after extinguishing at the Sensor

B. Residual Gas Component Patterns

Initial data is captured by the sensors and processed as a training set given the sensitivities of each sensor to component gases of the toxic emission (Table 1). We then extinguished the cigarette/vape, continued measuring sensor data for another 10–500 minutes to characterize cigarette smoke ‘residue’ post cigarette extinguishing (Figure 3). Classifiers using this data can detect cigarette smoke that lingers from the previous 24 hours after the cigarette was

extinguished – useful in hospitals, hotels, schools to classify toxicity of spaces to be used by different people.

C. Cigarettes Vs Burning Food

Emissions from Burning Food (Figure 4) are *relatively* harmless but trip conventional smoke/CO detectors anyways. Measurement data sets from burning food train the neural network to learn these patterns from burning food and discriminate it from Cigarette/Vape emissions

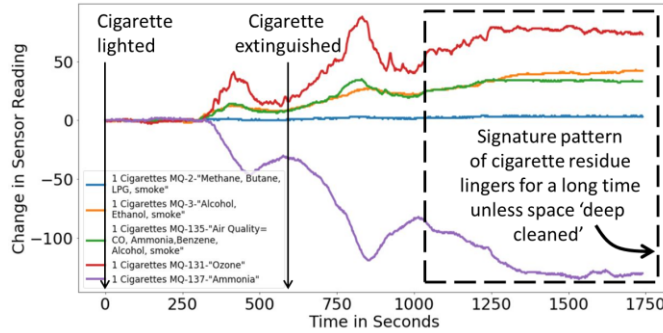


Figure 3. Cigarette emission residual component gases in room characterized for its signature pattern that persists long after cigarette extinguished.

Use of Pattern Recognition thus eliminates ‘False Alarms’ from CO detection in the ambient when conventional detectors are calibrated to trigger at low CO concentrations

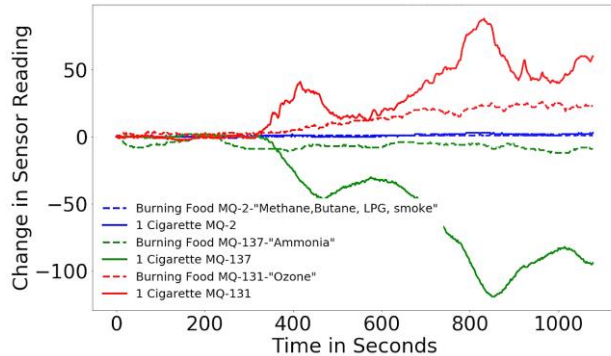


Figure 4: Classifier to discriminate Burning Food emissions from Cigarette emissions sensed by sensor array

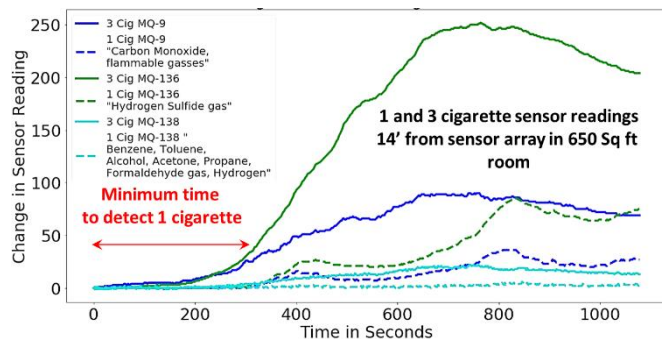


Figure 5. Speed of Source detection, reproducibility and consistency of Cigarette emissions Classifier demonstrated with measurements of 2 different levels of toxicity using the same source (Cigarettes).

D. Toxicity Level Classification

The Sensor array response to 1 cigarette is similar to emission from 3 Cigarettes emissions. Classifiers built using these measurements can discriminate between different levels of toxicity (Figure 5).

From the above observations, we demonstrate that cigarette smoke gas component density patterns at even small concentrations (from a single cigarette) that are detected by the sensors, are sufficient for the DNN to correctly classify the emission source as a cigarette – enabling a DNN based gas detection to be much faster than conventional smoke detectors that rely exclusively on CO gas concentration as the threshold for detection.

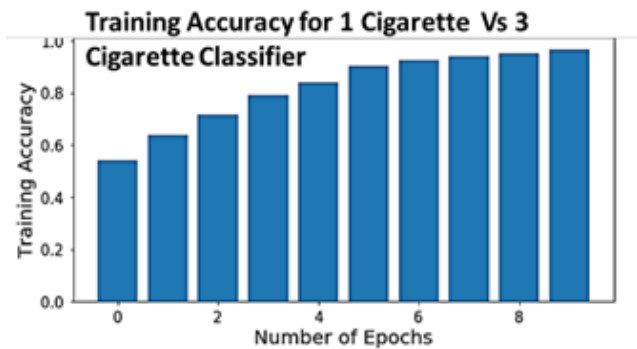
VI. ACCURACY OF CLASSIFIERS

The algorithm to train a DNN classifier is described in this section

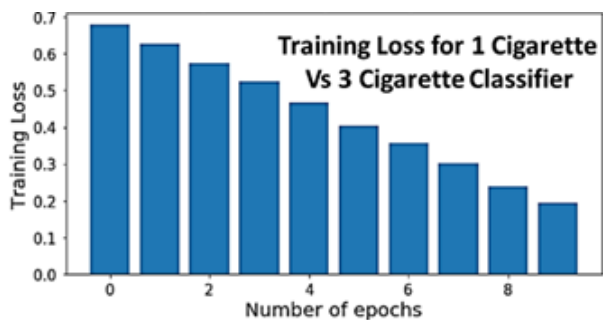
A. Training Loss and Accuracy of Classifier

To train a DNN classifier the training data has to be split into an “X_train” dataset and “Y_train” dataset. The “X_train” dataset consists of just the sensor readings as a function of time. The “Y_train” dataset consists only of the corresponding source name. While the DNN classifier was training on “X_train” and “Y_train” the classifier gave two different metrics: the training accuracy and the training loss, which were for each epoch. An epoch is one cycle through the full training data [9]. Three different classifiers were created. The first classifier was built to detect between 1 cigarette Vs 3 cigarette emissions (Fig 6a, 6b), the second was built to discriminate between 1 cigarette Vs 1 vape (Fig 7a, 7b), and the third was built to discriminate between a Cigarette or Vape Vs Burning food emissions (Fig 8a, 8b). The training accuracy reached >95% accuracy for all three classifiers (Figure 6b, 7b & 8b).

The training loss, which was calculated using binary cross-entropy, reached ~19% [Fig 7a] and ~10% [Fig 8a] after ten epochs for the first and second classifiers respectively. And for the third classifier, the training loss reached around ~8% (Figure 8a) after only 5 epochs. The training loss could have decreased to below 5% - however, to prevent the classifier from overfitting, the epochs were shortened up until the training loss for the third classifier reached a minimum of at least 10%. To test how well the classifier will perform on data it has never seen, the testing set was broken into the X_test and Y_test sets



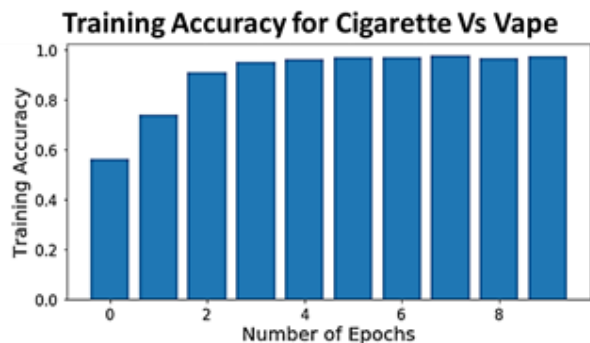
(a)



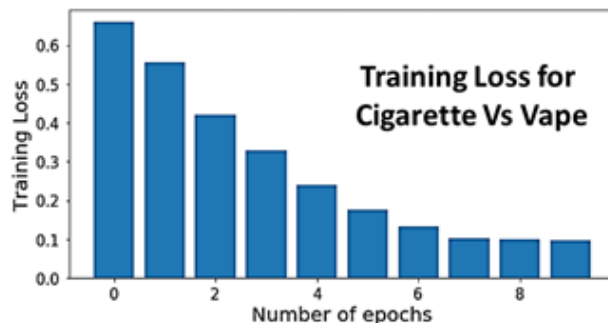
(b)

Figure 6. Training Vs Number of epochs in Classifier for 1 Vs 3 Cigarette emissions to discriminate Cigarette emissions at different levels of toxicity for (a) Accuracy and (b) Loss

The training loss, which was calculated using binary cross-entropy, reached ~19% [Fig 7a] and ~10% [Fig 8a] after ten epochs for the first and second classifiers respectively. And for the third classifier, the training loss reached around ~8% (Figure 8a) after only 5 epochs. The training loss could have decreased to below 5% - however, to prevent the classifier from overfitting, the epochs were shortened up until the training loss for the third classifier reached a minimum of at least 10%. To test how well the classifier will perform on data it has never seen, the testing set was broken into the X_test and Y_test sets.



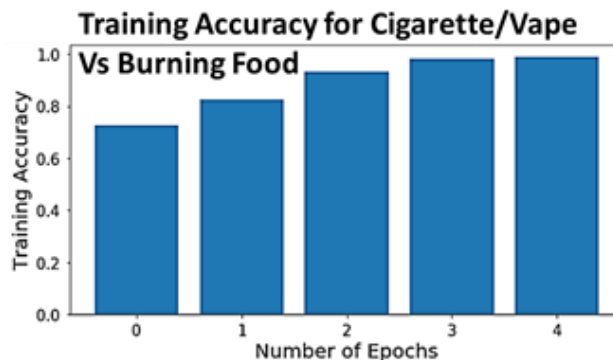
(a)



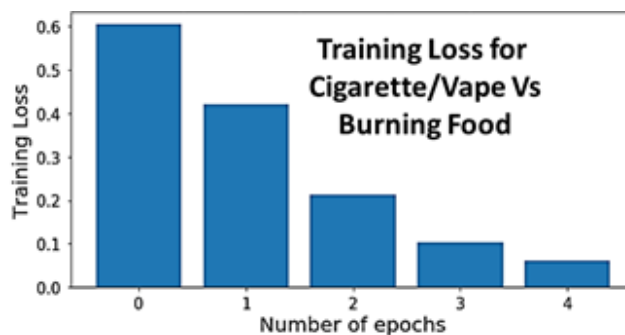
(b)

Figure 7: Training Vs Number of epochs in Classifier for Cigarette Vs Vape emissions to discriminate Cigarette emissions with similarly toxic emissions from Vape for (a) Accuracy and (b) Loss

The X_test only consists of never before seen data (by the classifiers) that only contains the sensor readings of the gases. The “Y_test” dataset only contains the corresponding sources of the “X_test”.



(a)



(b)

Figure 8: Training Vs Number of epochs in Classifier for Cigarette Vs Vape emissions to discriminate Cigarette emissions with similarly toxic emissions from Vape for (a) Accuracy and (b) Loss

The “X_test” was passed through the classifier and the resulting predictions are named “Y_predictions”. The “Y_predictions” and “Y_test” matched 100% accurately to each other. This is plausible given that the training accuracy reached >95% as shown in Figure 6b, 7b & 8b

VII. CONCLUSIONS AND FUTURE WORK

We demonstrate, using a simple inexpensive IoT system, equipped with an array of gas sensors and WiFi connectivity, the ability of a DNN to quickly identify a toxic gas by recognizing patterns in the concentrations of its component gases. These patterns are recognized at very low component gas concentrations *enabling a DNN based gas array sensor to provide early and accurate detection while toxic emissions still have low concentrations*. The DNN based detection is also limited only by the speed of toxic gas diffusion to the sensor arrays enabling the toxic gas detection to take place much sooner than conventional smoke/CO/gas sensor-based detectors

We see the need to extend these intelligent sensors to function as a distributed network of a few hundred IoT devices in a hospital or school for example, driving data wirelessly to a common AI hardware platform that could also support other AI workloads in the building as the use of AI proliferates.

ACKNOWLEDGMENTS

We would like to thank Mr. David Honeyford, Advisor of our *IoT Club* at Danbury High School and Mr. Jameson Parker, Advisor of our *AI Career Club* at Danbury High School. Both fantastic mentors taught us AP Physics. We would also like to thank Professor Hieu Nguyen, our ECE Faculty Research Advisor at the New Jersey Institute of Technology, Newark NJ for his encouragement and support.

REFERENCES

- [1] U.S. Department of Health and Human Services. The Health Consequences of Smoking—50 Years of Progress: A Report of the Surgeon General. 2014
https://www.cdc.gov/tobacco/data_statistics/sgr/50th-anniversary/index.htm, access on November 2020
- [2] U.S. Department of Health and Human Services. The Health Consequences of Involuntary Exposure to Tobacco Smoke: A Report of the Surgeon General. 2006
https://www.cdc.gov/tobacco/data_statistics/sgr/2006/index.htm, access on November 2020
- [3] [https://www.nfpa.org/News-and-Research/Data-research-and-tools/US-Fire-Problem/Smoking-Materials#:~:text=One%20in%2020%20home%20\(5,year%20period%20of%202012%2D2016](https://www.nfpa.org/News-and-Research/Data-research-and-tools/US-Fire-Problem/Smoking-Materials#:~:text=One%20in%2020%20home%20(5,year%20period%20of%202012%2D2016). Access on November 2020
- [4] A. Dey, “Semiconductor metal oxide gas sensors: A review”, Materials Science & Engineering B, Vol 229 March 2018, pg 206 – 217. Elsevier
- [5] <https://support.google.com/googlenest/answer/9330256?hl=en>, access on November 2020
- [6] <https://towardsdatascience.com/why-data-should-be-normalized-before-training-a-neural-network-c626b7f66c7d>, access on November 2020
- [7] www.mysensors.org/build/gas, access on November 2020
- [8] J. Moolayil, “A Layman's Guide to Deep Neural Networks.” Medium, Towards Data Science, 30 May 2020, towardsdatascience.com/a-laymans-guide-to-deep-neural-networks-ddcea24847fb. Access on November 2020
- [9] deeptai.org/machine-learning-glossary-and-terms/epoch Access on November 2020

IMPAQT Miniaturized Underwater Acoustic Telemetry Platform: Transmitter Node System Design

Hamed Jafarzadeh
Tyndall National Institute
University College Cork
Cork, Ireland
e-mail: hamed.jafarzadeh@tyndall.ie

Marco Belcastro
Tyndall National Institute
University College Cork
Cork, Ireland
e-mail: marco.belcastro@tyndall.ie

Brendan O’Flynn
Tyndall National Institute
University College Cork
Cork, Ireland
e-mail: brendan.oflynn@tyndall.ie

Abstract—The marine environment and its natural resources are an essential part of the geographical ecosystem and a great food source for humans. In recent years, terrestrial wireless sensor networks and Internet of Things (IoT) technologies have developed rapidly; however, due to the limitation of signal propagation in water, there is less development and advancement in the underwater sensors network domain. IMPAQT is a European research project aiming at the development of the technologies and methods to promote and support inland, coastal zone and offshore Integrated Multi-Trophic Aquaculture (IMTA) sites. As part of the IMPAQT project, a novel underwater acoustic telemetry platform has been proposed and is under development, to provide a method to collect and transmit sensors data underwater. The proposed platform architecture consists of several ultrasonic transmitter sensor nodes and a gateway buoy as a data aggregator interface. Transmitter nodes will collect and log underwater sensor data and transmit it at regular intervals to the gateway buoy and the gateway buoy will send the collected data to a data management system using a Long Range (LoRa) communication link. The IMPAQT Transmitter node has an integrated accelerometer sensor, a temperature sensor, and a pressure sensor onboard. There is also an Infrared Data Association protocol (IrDA) interface that can be used to attach any external auxiliary sensor module to the transmitter node and configure the transmitter node to collect the external module’s data. The current version of the transmitter node under development can be attached to seaweed, or it can be used as a floating sensor node in the water and due to its small size and weight design it almost has no impact on the working environment. In this paper, the background of the miniaturized underwater sensors is studied, and design method of the transmitter node is discussed. Future work will focus on the test and deployment of the transmitter and gateway in marine deployments.

Keywords- *Biotelemetry; Underwater communication; Underwater sensors network; underwater sensor node;*

I. INTRODUCTION

According to the latest United Nations world population estimation, by the year 2050, the population of the earth will reach approximately 10 billion people [1], and this increase will result in higher demand for food and consequently seafood as it is one of the main source of food and nutrition for many people. In the past, capture fisheries productions

were the primary source of the seafood, but this has been changed in 2012, where aquaculture production volumes exceeded that of the capture fisheries, and it is seen to be increasing rapidly in recent years to meet demand [2]. To provide more sustainability, reduce environmental impacts, and promote economic gains, integrated multi-trophic aquaculture (IMTA) is gaining popularity among marine farmers. In IMTA, farmers combine fed species (e.g., fish, shrimp, oysters) with extractive species (e.g., seaweed, mussels), and extractive species will use the by-products of the fed species, reducing the environmental impact of the sites and also to provide commercial profit to the farmers.

IMPAQT is a European project aimed at promoting and supporting the development of IMTA sites by providing a multi-purpose, multi-sensing, and multi-functional data management platform. To provide accurate and relevant information about the underwater environment, a novel miniaturized low-power and low-cost underwater transmitter node and a gateway buoy receiver have been proposed and is being evaluated to collect information from sensors and transmit it to the inland data aggregators. The transmitter node has integrated onboard sensors, and it is capable of interfacing with external sensor modules using the optical IrDA protocol.

The IMPAQT underwater telemetry platform is an ongoing project, and currently, various design parameters and solutions are under evaluation and development.

In section II, the current state of the related research projects studied. Section III describes the development of the transmitter node circuit, design parameters and, also power analysis of the circuit. Section IV addresses the current state of the project and plans for improvements.

II. BACKGROUND AND RELATED WORK

With the rapidly increasing and evolving aquaculture market sector, it is essential to monitor and analyze the effects of the methods that have been used in aquaculture, to reduce the costs and improve stability and sustainability of the sites. There is experimental monitoring in the labs and tanks. However, due to the differences between the experimental environment and real aquaculture environments, it is hard to compare accurately, especially when it comes to the biasing

caused by the handling of marine animals [3]. In [4], authors proposed the concept of Precision Fish Farming intending to use scientific methods to manage the fish production by enabling farmers to monitor, control and document the biological process in fish farms. With the advancement of chemistry and electrical sensing technologies, it is now possible to develop miniaturized attached sensor devices to track and study the natural behaviour of marine animals and plants in their cultural environment.

To achieve the goal mentioned earlier, in [5], authors describe the development of an ultra-low-power sensor device, AE-FishBIT, for monitoring physical activities and respiratory frequency of the farmed fish, using the onboard accelerometer sensor, attached to the fish, and logging the sensors' information. *AE-FishBIT* is not able to transmit the data, and the fish is required to be captured to download the sensors data, however, due to its form factor and size, it is easy to attach and detach the device to the operculum of the fish. Almeida et al. [6] monitored the behaviour of Lusitanian toadfish using accelerometry data provided by the externally attached *AccelTag*, which was able to log, recognize and transmit behaviour type of the fish.

There are also devices for tracking the movement of the fish in dams, fisheries, and cages, shown in Figure 1. In [7], authors have developed the Juvenile Salmon Acoustic Telemetry System (*JSATS*), to identify and track the movement of juvenile salmon in dams and rivers. *JSATS* tags are extremely compact, with a length of 15mm and a diameter of 3.38mm, which allows them to be injected using a needle into the body of the fish. They can transmit ultrasonic pings for a year with a 15-second ping interval. But *JSATS* tags are only capable of transmitting a pre-programmed unique identification code and temperature data, and they are not able to provide any other sensor data.

Another method to monitor the marine environment is to use unmanned underwater vehicles. SeaSmart has introduced three patented wireless drones to collect environmental data, for instance, oxygen, salinity, biomass, and temperature, by travelling through the cage to collect data and returning to surface to transmit the collected information. [8].

There are also efforts on monitoring IMTA and aquaculture sites using remote sensing technologies, in [9], authors have used multi-sensor (satellite, unmanned aerial vehicle, and ground spectroradiometer) remote sensing techniques to monitor seaweed aquaculture in the Yellow Sea.

III. MATERIALS AND METHOD

The focus of IMPAQT telemetry project is on IMTA sites, where all sensors will be deployed in a bounded area, and it is considered that the gateway buoy will be in a maximum distance of 100m from each sensor tag.

In Figure 2, the IMPAQT telemetry system is shown, and in this paper, the design method of the transmitter node will be discussed. The goal of the transmitter is to transmit sensors data provided by its internal sensors or externally

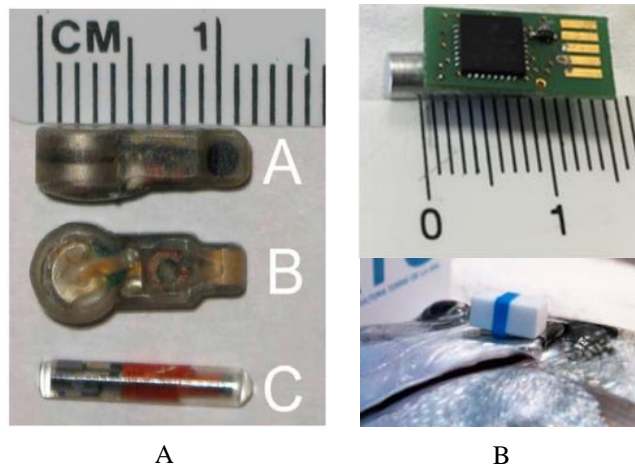


Figure 1. (A) JSATS Tags (B) AE-FishBIT tags

connected sensor to the gateway buoy using acoustic waves. The IMPAQT transmitter node needs to be miniaturized to minimize its impact on the deployment environment. Considering the size and power consumption of the tag, accordingly, the block diagram design in Figure 3, and associated system design is suggested. Regarding the receiver aspect of the transceiver system, the buoy mounted gateway board is an application specific system designed in conjunction with the transmitter board described in detail in this publication. It is anticipated that the full transceiver system (gateway and transmitter) and its deployment will be described in full in a follow on publication.

A. Transducer material selection

PZT materials are one of the most widely used piezoelectric materials, and they have been used in different applications, in particular as fish tags [6][7][10]. In [11], four types of PZT materials' (Customized Type VI, Type VI, Type I and Type II) energy consumption, source-level, and frequency response has been compared. From the energy consumption aspect, PZT Type VI consume more energy comparing to other types, but they also provide better source level and frequency response compared to others. By comparing the results, type VI had a good balance between the source level and power consumption; consequently, for designing the JSATS tags, they have used PZT Type VI material.

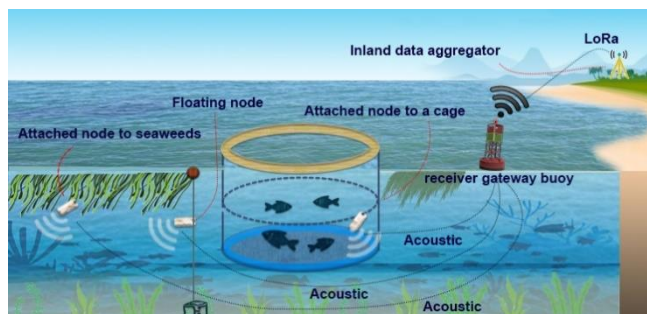


Figure 2. IMPAQT telemetry platform

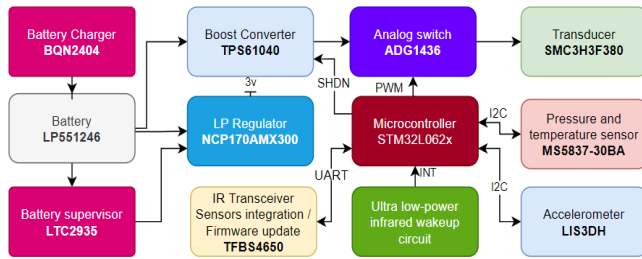


Figure 3. Block diagram of IMPAQT Acoustic Transmitter Node

For IMPAQT transmitter tags, a PZT type VI (*SMC3H3F380*) from *STEMiNC Inc*, with an outer diameter of 3mm and height of 3mm, with the resonance frequency of 380 KHz \pm 15KHz has been selected.

B. Transducer driver

To estimate the required driving voltage for the piezo transducer to provide sufficient detection range, it is necessary to study underwater acoustic models and signal absorption loss. The sound emitted by the piezo transducers is attenuated by two main factors, viscous absorption factor, and chemical relaxation effect. The selected piezo material resonance frequency is at 380KHz, and at this frequency, viscous absorption and magnesium sulphate relaxation effect is significant, which can be estimated by the following simplified formula [12] :

$$\alpha = 0.106 \frac{f_1 f^2}{f^2 + f_1^2} e^{(pH-8)/0.56} + 0.52 \left(1 + \frac{T}{43} \right) \left(\frac{S}{35} \right) \frac{f_2 f^2}{f^2 + f_2^2} e^{-z/6} + 0.00049 f^2 e^{-\left(\frac{T}{27} + \frac{z}{17}\right)} \quad (1)$$

Where in the proposed design and operating environment, $f=380\text{KHz}$ (Piezo resonance frequency), $T = 8^\circ\text{C}$ (water temperature), $S = 35\text{ppt}$ (seawater salinity), $\text{pH} = 8.1$ (current ocean pH level [13]), $z = 50\text{m}$ (estimated working depth), and relevant relaxation frequencies are:

$$f_1 = 0.78 \left(\frac{S}{35} \right)^{\frac{1}{2}} e^{\frac{T}{26}} \quad (\text{for boron}), \quad (2)$$

$$f_2 = 42 e^{\frac{T}{17}} \quad (\text{for magnesium}). \quad (3)$$

Using (1) by substituting the parameters, the absorption loss of 92.4 dB per kilometer has been estimated for an infinitely narrow acoustic beam, however, practical beams spread as they propagate through the water, in order to mitigate the spreading loss, (4) can be used for the transmission loss at the distance of R [14]:

$$TL = TL_1 + \alpha R, \quad (4)$$

$$TL_1 = 20 \log R, \quad (5)$$

In the IMPAQT project, a maximum distance of 100m is considered between the transmitter and receiver nodes, which leads to an overall transmission loss of 49.2 dB at 100m.

To provide an adequate sound level, a voltage booster circuit has been implemented using TPS61040 controller, which can boost the 2.5-3.7v (LiPo cell voltage) up to 28v.

The average current of the piezo transducer can be estimated by (6) [15] :

$$I_{Avg} = \frac{2Q}{T} = 2CVf \quad (6)$$

Where Q = Charge in the piezoelectric transducer, T =Period of the driving signal, $C=70\text{pF}$ (Static capacitance), $V = 20\text{v}$ (Driving voltage), $F = 380\text{KHz}$ (Resonance frequency). Using the parameters of the selected piezo material, the average current would be about 1mA.

The tag's sound level can be programmed using the IrDA interface based on the use case. ADG1438 analog switch IC has been used to drive the piezo terminals at the boosted voltage using PWM modulation provided by the microcontroller.

C. Sensors and external interface

An accelerometer sensor (LIS3DH), and a pressure and temperature sensor (MS5837-30BA) are included in the IMPAQT transmitter tag to monitor the aquaculture environment and tag movement. TFBS4650 is also selected as the external sensors interface, where auxiliary sensor boards and modules can communicate with the transmitter tag to transmit their sensor value to the gateway buoy, at real-time or at predefined intervals. External sensor modules can also trigger the tag's microcontroller to wake up and read the external sensors data using the low-power infrared wake-up circuit. The evaluation boards and IrDA transceiver have been shown in Figure 4.

D. Power consumption and battery management

The transmitter tag runs on a 260mAh LiPo battery (Part number:LP551246). There is a compact battery charger and a battery supervisor circuit on the board, to charge and cut off the battery in the case of full discharge.

Considering the 260mA battery, total sleep current of 6.34uA (refer to Table I which is based on data available on individual product datasheets), the maximum current of about

TABLE I COMPONENTS POWER CONSUMPTION

Component	Sleep current (μA)	Typical supply current (μA)	Max supply current (μA)
BQ24040	1	1	6
LTC2935	0.5	0.5	0.5
TPS6104	1	25	25
NCP170AMX300	0.5	0.9	0.9
TFBS4650	0.01	75	2000
ADG1436	1	170	280
STM32L062x	0.23	312	780
MS5837-30BA	0.1	20	1250
LIS3DH	2	2	11
Piezo	0	1000	1000

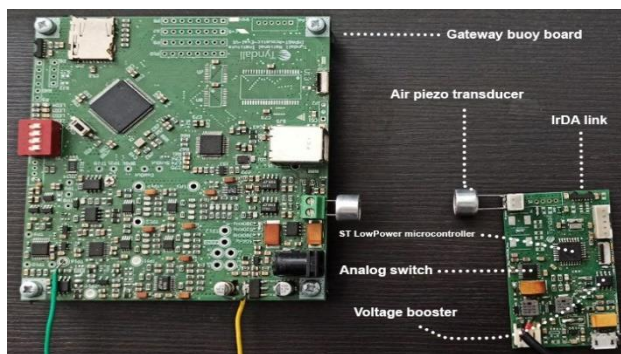


Figure 4. IMPAQT telemetry platform evaluation board

5.3 mA when sampling all sensors, and about 1.6mA while transmitting the data, based on user configuration the battery life can last from two weeks to three months.

To maximize the battery life, the tag can be programmed via IrDA interface to wake up and read the sensors data at regular intervals, while also an external sensor or module can force the tag to wake-up using the wake-up circuit.

IV. CONCLUSION AND FUTURE WORK

The proposed telemetry method, using a transmitter and a gateway buoy can help farmers and researchers to monitor and analyze underwater water environment. The proposed transmitter tag incorporates an accelerometer, a temperature sensor and a pressure sensor. However, the main novelty of this work is its size and that it is designed to be attachable to other sensors and modules. This project is a work in progress, and it is considered to improve aquaculture sites monitoring as a part of IMPAQT project, which is ongoing.

Currently, the transceiver system prototype boards, shown in Figure 4, have been developed and evaluated in air and 200 bit per second achieved using binary phase-shift keying and On-Off keying modulations at 40KHz frequency. It is expected that by using 380KHz piezo materials, the bitrate will increase significantly, which will reduce the overall battery consumption and lead to more frequent data capturing and transmitting. Based on the components that have been selected, it is estimated that the final dimension of the tag would be less than 5 cm x 2 cm x 2 cm. This system will be tested in an aquatic environment and reported on in a subsequent publication.

In future, more studies can be done on the optimization of the battery consumption, bitrate improvement and more miniaturized design. Also, there would be an opportunity to connect the tag to the sensors developed by other colleagues in IMPAQT project to provide a better understanding of underwater environments.

ACKNOWLEDGMENTS

This work is part of IMPAQT project (<https://impactproject.eu/>) – and it has received funding from the European Union’s Horizon 2020 research and innovation programme under Grant Agreement No 774109. Aspects of

this publication have been funded in part by a research grant from Science Foundation Ireland (SFI) - co-funded under the European Regional Development Fund under Grant Number 16/RC/3835 – VISTAMILK and 13/RC/2077 - CONNECT.

REFERENCES

- [1] “World Population Prospects - Population Division” <https://population.un.org/wpp/Graphs/DemographicProfiles/Line/900> [retrieved: Sep, 2020].
- [2] “Seafood production: wild fish catch vs aquaculture,” *Our World in Data*. <https://ourworldindata.org/grapher/capture-fisheries-vs-aquaculture-farmed-fish-production> [retrieved: Sep, 2020].
- [3] E. Baras and J.-P. Lagardère, “Fish telemetry in aquaculture: review and perspectives,” *Aquac. Int.*, vol. 3, no. 2, pp. 77–102, Jun. 1995, doi: 10.1007/BF00117876.
- [4] M. Føre *et al.*, “Precision fish farming: A new framework to improve production in aquaculture,” *Biosyst. Eng.*, vol. 173, pp. 176–193, Sep. 2018, doi: 10.1016/j.biosystemseng.2017.10.014.
- [5] J. A. Martos-Sitcha *et al.*, “Ultra-Low Power Sensor Devices for Monitoring Physical Activity and Respiratory Frequency in Farmed Fish,” *Front. Physiol.*, vol. 10, 2019, doi: 10.3389/fphys.2019.00667.
- [6] P. R. de Almeida, T. J. Pereira, B. R. Quintella, A. Gronningsaeter, M. J. Costa, and J. L. Costa, “Testing a 3-axis accelerometer acoustic transmitter (AccelTag) on the Lusitanian toadfish,” *J. Exp. Mar. Biol. Ecol.*, vol. 449, pp. 230–238, Nov. 2013, doi: 10.1016/j.jembe.2013.09.015.
- [7] T. N. Pearsons, “The Juvenile Salmon acoustic telemetry system : a new tool,” *Fisheries*, vol. 35, no. 1, pp. 23–31, Jan. 2010, doi: 10.1577/1548-8446-35.1.23.
- [8] “SeaSmart AS (EN).” <https://www.seasmart.no/english.html> [retrieved: Oct, 2020].
- [9] C. C. Krueger *et al.*, “Acoustic telemetry observation systems: challenges encountered and overcome in the Laurentian Great Lakes,” *Can. J. Fish. Aquat. Sci.*, vol. 75, no. 10, pp. 1755–1763, Dec. 2017, doi: 10.1139/cjfas-2017-0406.
- [10] R. B. Mitson and T. J. Storeton-west, “A transponding acoustic fish tag,” *Radio Electron. Eng.*, vol. 41, no. 11, pp. 483–489, Nov. 1971, doi: 10.1049/ree.1971.0147.
- [11] H. Li, Z. D. Deng, Y. Yuan, and T. J. Carlson, “Design parameters of a miniaturized piezoelectric underwater acoustic transmitter,” *Sensors*, vol. 12, no. 7, pp. 9098–9109, 2012, doi: 10.3390/s120709098.
- [12] M. A. Ainslie and J. G. McColm, “A simplified formula for viscous and chemical absorption in sea water,” *J. Acoust. Soc. Am.*, vol. 103, no. 3, pp. 1671–1672, Mar. 1998, doi: 10.1121/1.421258.
- [13] “Ocean Acidification | Smithsonian Ocean.” <http://ocean.si.edu/ocean-life/invertebrates/ocean-acidification> [retrieved: Oct, 2020]
- [14] “Forming the acoustic equations” <http://www.fao.org/3/X5818E/x5818e05.htm> [retrieved: Oct, 2020]
- [15] “Please tell me a current consumption by a Piezoelectric Sounder (External Drive Type). | Murata Manufacturing Co., Ltd.” <https://www.murata.com/en-us/support/faqs/products/sound/sounder/char/sch0003> [retrieved: Oct, 2020].